

IMPERIAL

Numerical Simulation of the SPLEEN Low Pressure Turbine Cascade using Nektar++

Author

Mateusz Dominik Lisiewski
CID: 01954031

Supervised by

Prof. Spencer J. Sherwin

A Thesis submitted in fulfillment of requirements for the degree of

**Master of Advanced Computational Methods for Aeronautics,
Flow Management and Fluid-Structure Interaction**

Department of Aeronautics
Imperial College London
2025

Acknowledgements

I would like to express my gratitude to those who have supported me throughout this project. First, to my supervisor, Professor Spencer J. Sherwin, for this invaluable guidance, kindness and constant support – even from a distance. To Dr Guglielmo Vivarelli, thank you for your patience with my questions and for always adding a practical perspective to our discussions. I am deeply grateful to my parents and family for their constant encouragement and faith in me. Finally, to my peers, thank you not only for sharing the deadlines and study sessions, but more importantly much-needed evenings at the Union bar.

I acknowledge the use of ChatGPT 5 (OpenAI, <https://chat.openai.com/>) as a supplementary tool to support my understanding of relevant material and to assist in debugging Nektar++ and Python. I confirm that no content generated by AI has been presented as my own work.

Contents

1	Introduction	2
2	Literature Review	3
2.1	Low Pressure Turbine	3
2.2	Numerical Simulations of LPTs	3
2.3	Artificial Viscosity	5
2.4	Project Aim and Objectives	6
3	Numerical Methods	6
3.1	Spectral/hp element method	6
3.2	Governing Equations	9
3.3	Non-dimensionalisation Strategy	10
3.4	Artificial Viscosity	10
4	Problem Formulation	11
4.1	Domain Geometry and Mesh	11
4.2	Parameters and Boundary Conditions	14
4.3	Solver Configuration	14
4.4	Conservative Variables	15
4.5	Convergence and Time Averaging	15
4.6	Simulation Workflow	16
5	Results	17
5.1	Flow Physics	17
5.1.1	Flow Field Analysis	17
5.1.2	Blade Loading	19
5.1.3	Skin Friction	22
5.1.4	Outlet Mach number	24
5.1.5	Numerical Bubble	24
5.2	Artificial Viscosity Study	25
5.2.1	Finding the Optimum Value	25
5.2.2	Polynomial Order Influence	26
5.3	Effect of Dimensionality	28
6	Conclusion and Future Work	32
6.1	Conclusion	32
6.2	Future Work	33
A	Solver Settings	37
B	Star-CCM+ Wake	38
C	Artificial Viscosity Study Supplement	39
D	Star-CCM+ Tutorial	40

List of Figures

1	GE9X engine section view from [8]. HSLPT is highlighted in orange.	3
2	Discontinuous Galerkin interface treatment from [30].	7
3	Blade geometry illustration from [33] and corresponding parameters from [7]. . .	12
4	Computational domain and mesh with zoom on refinement regions.	12
5	Near-wall resolution ($P = 4$).	13
6	Statistical convergence assessment. <i>Time</i> denotes convective time units (CTU). .	15
7	Simulation and post-processing workflow.	16
8	Mach number in the passage.	17
9	Instantaneous Mach number visualisation after 40 CTUs.	18
10	Compressibility effects. White contours correspond to $M = 1$	19
11	Time-averaged isentropic Mach number ($M_{out} = 0.7$).	20
12	Time-averaged isentropic Mach number ($M_{out} = 0.9$).	21
13	Time-averaged isentropic Mach number ($M_{out} = 0.95$).	22
14	Time-averaged skin-friction coefficient along the blade.	23
15	Pressure-surface numerical bubble ($M_{out} = 0.95$, $P = 4$).	25
16	Key flow features with no AV added.	25
17	Key flow features with high AV added.	26
18	AV result variation with P . Note that AV applied at shock is marked in orange. Results for a single domain are presented for better visibility.	27
19	Results for the optimum AV settings.	28
20	Time-averaged isentropic Mach number comparison between dimensional and non-dimensional setups for two polynomial orders ($M_{out} = 0.95$).	28
21	Time-averaged outlet Mach number. <i>Average</i> is the space average.	29
22	Instantaneous dimensional (left) and non-dimensional (right) quantities after 40 CTUs. Only two extruded domains were shown for visibility.	30
23	AV applied for dimensional (left) and non-dimensional (right) setups.	31
24	Modal energy evolution. <i>Time</i> on the x-axis denotes CTU.	32
25	Wake Resolution from Star-CCM+ simulation ($M_{out} = 0.95$), showing the char- acteristic smooth, triangular wake with no unsteady oscillation.	38
26	Mach number visualisations for dimensional (left) and non-dimensional (right) setups at different CTUs. One domain shown for visibility. The poor result quality is attributed to the fact that the simulations were run for $P = 1$	39

List of Tables

1	Typical near-wall grid spacing requirements for LES and DNS from [36].	13
2	Simulation parameters for three cases.	14
3	Errors in outlet Mach number prediction.	24
4	<i>SolverInfo</i> part of the Nektar++ session file.	37

Nomenclature

Abbreviations

AV	Artificial Viscosity	γ	Ratio of specific heats
BL	Boundary Layer	κ	Sensor sharpness parameter
CFD	Computational Fluid Dynamics	μ	Dynamic viscosity
CFL	Courant–Friedrichs–Lowy (number)	μ_0	Artificial viscosity (Nektar++)
CTU	Convective Time Unit	ν	Kinematic viscosity
DG	Discontinuous Galerkin	ρ	Density
DNS	Direct Numerical Simulation	ε	Artificial viscosity
HPT	High Pressure Turbine	c	True chord
HSLPT	High-Speed Low Pressure Turbine	c_f	Skin friction coefficient
ILES	Implicit Large Eddy Simulation	E	Total energy
LDG	Local Discontinuous Galerkin	g	Blade pitch
LE	Leading Edge	h	Element size
LES	Large Eddy Simulation	k	Thermal conductivity
LPT	Low Pressure Turbine	P	Polynomial order
ML	Machine Learning	p	Pressure
PDE	Partial Differential Equation	R	Gas constant
PS	Pressure Surface	S	Surface coordinate
RANS	Reynolds-Averaged Navier Stokes	s_κ	Sensor threshold parameter
SIPG	Symmetric Interior Penalty Galerkin	s_e	Smoothness indicator
SS	Suction Surface	S_L	Surface length
TE	Trailing Edge	T	Temperature
URANS	Unsteady Reynolds-Averaged Navier Stokes	u, v	Velocity components

Physical Constants

α	Flow angle	∞	Freestream value
Δt	Timestep	in	Inlet value
Δx^+	Streamwise mesh resolution	out	Outlet value
Δy_{wall}^+	Wall-normal mesh resolution	M	Mach number
		M_s	Isentropic Mach number
		Re	Reynolds number

Abstract

This thesis examines the application of the spectral/hp element solver Nektar++ to the SPLEEN high-speed low-pressure turbine cascade, with specific focus on the assessment of artificial viscosity as a stabilisation strategy. Previous turbomachinery studies using Nektar++ have predominantly relied on incompressible formulations and the canonical T106A cascade; the present work extends validation to a compressible configuration representative of geared turbofan operating conditions. Simulations at outlet Mach numbers of 0.7, 0.9 and 0.95 demonstrate satisfactory agreement with experimental data and improved performance relative to a RANS baseline from Star-CCM+. Nektar++ captures the essential compressible flow behaviour with higher fidelity than Star-CCM+, although pressure-side predictions are compromised by a numerical separation bubble, attributed to the absence of inflow turbulence, consistent with other high-order studies.

The artificial viscosity investigation provides initial guidelines for tuning stabilisation parameters and demonstrates that higher polynomial orders may inadvertently increase dissipation due to reduced activation thresholds. This highlights the need for a more informed methodology for selecting artificial viscosity parameters, ensuring sufficient local stabilisation without introducing excessive smoothing in other regions. The principal novelty of the study is the implementation of a dual-setup strategy, enabling direct comparison of dimensional and non-dimensional formulations. This approach reveals non-trivial discrepancies in artificial viscosity activation and shock resolution, with results indicating that numerical artefacts associated with scaling choices may influence the observed behaviour.

The findings confirm the suitability of Nektar++ for compressible turbomachinery flows and establish methodological recommendations for the effective use of artificial viscosity within the compressible solver framework.

1 Introduction

Advancement in propulsion technology requires detailed, insightful, and accurate analysis of each part of the jet engine - from inlet to nozzle - and throughout its entire lifecycle. Numerical simulations play a central role in turbomachinery development [1], yet they can become a bottleneck, often requiring days to complete [2]. To accelerate innovation, engineers require simulation tools that offer both greater robustness and improved accuracy.

Although initially adopting Computational Fluid Dynamics (CFD) enabled aerospace manufacturers, such as Boeing or Pratt & Whitney, to significantly decrease the number of wind tunnel and rig tests, the advancement has somewhat plateaued in the early 2000s [3]. This is, among others, attributed to insufficient accuracy of turbulence modelling approaches [1], which are often too simplistic to capture complex flow physics with sufficient fidelity. Methods such as Reynolds-Averaged Navier-Stokes (RANS) or Unsteady RANS (URANS) provide approximate solutions by simplifying the governing equations through time-averaging of the turbulent fluctuations. However, this comes at the cost of accuracy, as the equations no longer represent the full flow physics but rather a simplified model that can miss critical flow features. Given the complex mixing processes and inherently unsteady nature of turbomachinery flows, accurate numerical description of the underlying physics is key [1]. Employing more accurate simulations, such as Direct Numerical Simulations (DNS) or Large Eddy Simulations (LES), would enable significant improvements in the design and optimisation of turbomachinery components, but resolving the turbulent unsteady flow was shown to be more than 100 times more computationally expensive than RANS and URANS [4].

Spectral/hp element methods offer a viable alternative to conventional CFD approaches, enabling the move from the current low-fidelity RANS practice towards fully-resolved DNS. By combining mesh refinement with variable polynomial order, these methods effectively capture essential turbulent structures, achieving substantially reduced solution errors [5]. However, their low inherent dissipation makes them susceptible to numerical instabilities in the presence of shocks or sharp gradients. Artificial viscosity (AV) provides a stabilisation mechanism by locally increasing dissipation where needed, allowing accurate shock resolution without degrading smooth regions of the flow. Such control over numerical dissipation and dispersion characteristics is particularly crucial with tight error requirements, such as enabling high-fidelity turbomachinery analysis and design. Through rigorous validation against experimental data, this study investigates whether spectral/hp element methods can become the new standard for capturing the intricate dynamics of turbomachinery flows.

2 Literature Review

2.1 Low Pressure Turbine

Jet engines are the primary propulsion system for modern commercial aircraft. A typical turbofan (Figure 1) comprises a fan, multi-stage compressor, combustor, turbine and nozzle. The turbine extracts energy from the high-temperature, high-pressure gas to drive the upstream compressor and fan via one or more shafts. This study focuses on the low pressure turbine (LPT), which lower Reynolds number compared to the high-pressure turbine (HPT) makes it more suitable for cost-effective high-fidelity simulations. In conventional designs, the LPT rotational speed is constrained by the fan, which cannot operate at excessive tip speeds to avoid noise and excessive structural stresses [6]. The introduction of geared turbofan engines decouples the fan and LPT through a reduction gearbox, allowing the LPT to run at higher rotational speeds. This increases the workload per stage and consequently reduces the required number of stages, lowering specific fuel consumption and improving the overall fuel efficiency [6]. While conventional LPTs are well documented, high-speed LPTs (HSLPT) remain largely unexplored [7]. This study addresses that gap and demonstrates how to tune the Nektar++ solver to reliably capture the unique flow in HSLPTs.

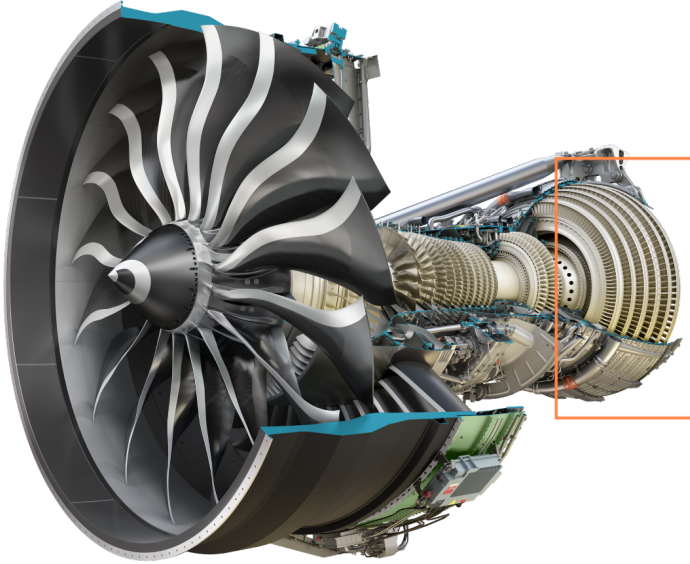


Figure 1: GE9X engine section view from [8]. HSLPT is highlighted in orange.

2.2 Numerical Simulations of LPTs

In the past years, several studies have evaluated the performance of higher-order CFD methods at industrial Reynolds numbers, demonstrating that implicit LES (ILES) or DNS simulations are viable. For example, Garai et al. carried out DNS of the T106A turbine cascade at Reynolds numbers up to 200000. They found good agreement with experimental results, attributing the discrepancies primarily to the absence of prescribed inflow turbulence [9]. In another investi-

gation of the T106A cascade, Vincent et al. showed that the high-order CFD solver PyFR is capable of performing ILES and reproduce experimental isentropic Mach number distributions with close agreement. They argued that such simulations could enable full-scale virtual LPT cascade capability, reducing the reliance on experimental campaigns and providing detailed data to improve LES and RANS turbulence models [10]. More recently, Borbouse et al. applied the ArgoDG solver to the SPLEEN LPT cascade, reporting reasonable agreement with the experiments while also discussing the influence of compressibility on the flow field [7]. These results underscore the suitability of high-order methods for turbomachinery flows. Building on this evidence, the following paragraph summarises studies evaluating the spectral/hp element solver Nektar++, which is employed in the current work.

The suitability of Nektar++ to turbomachinery analysis has been documented in several publications. Vivarelli et al. presented a comprehensive review of incompressible and compressible capabilities, reporting simulation results for jet-engine intake, fan, LPT and HPT [11]. In another paper, Vivarelli et al. performed a 2.5D study of a compressor blade with separation bubbles and inflow turbulence, demonstrating that extrusion-based meshing approach can accurately capture natural transition mechanisms and that the flow field is sensitive to turbulence intensity [12]. For LPTs, Cassinelli et al. published a series of incompressible simulations on the T106A turbine cascade, quantifying inflow disturbance effects [13,14], and later extended their work to investigate wake passing effect in a LPT [15]. Using the same geometry Cassinelli et al. established best-practice guideline for Nektar++ LPT simulations, covering P -refinement, flow features analysis, spanwise extrusion and convergence assessment for spectral/hp element methods [16]. For completeness, related Nektar++ work on turbulence injection [17], sliding-mesh method for moving geometries [18], and ML-assisted RANS modelling [19 and 20] have been reviewed; these inform context but are not central to the present study.

This overview demonstrates the wide range of turbomachinery applications in which Nektar++ has been validated. However, nearly all LPT studies so far rely on the incompressible formulation, even though real LPTs can operate in compressible regimes. This is problematic because neglecting compressibility effects can incorrectly capture shock location and mischaracterise loss mechanisms. Moreover, validation has largely focused on the canonical T106A cascade; extending benchmarking to other geometries would strengthen confidence in Nektar++'s suitability for turbomachinery studies. To address these gaps and frame the subsequent discussion, the literature review for the studied turbine cascade - SPLEEN LPT - is now presented.

The SPLEEN high-speed LPT cascade has been investigated experimentally and numerically in several papers. As mentioned earlier, Borbouse et al. investigated the compressibility effects on the flow field without inlet turbulence, reporting reasonable agreement with the experiments [7]. In a subsequent study, Nathan Deneffe investigated the influence of injected turbulence on the SPLEEN cascade flow and reported improved agreement with experimental data [21].

Building on this, Maxime Borbouse and Nathan Deneffe investigated the SPLEEN geometry in RANS simulations using the open-source CFD solver SU2, reporting that Spalart–Allmaras turbulence model performed particularly well [22]; consequently the Spalart–Allmaras model was adopted for the Star-CCM+ RANS simulations in this work. On- and off-design conditions of the SPLEEN LPT cascade at engine-relevant Reynolds and Mach numbers were studied experimentally in a two-part paper: Simonassi et al. describe the component and instrumentation design [23], and Lopes et al. report the aerodynamic behaviour at on- and off-design flow conditions [24]. These investigations form the primary reference for this study.

2.3 Artificial Viscosity

SPLEEN LPT cascade operates at high speeds, which may lead to shocks in the domain. For that reason, a shock-capturing strategy compatible with high-order discretisations is required to resolve the discontinuities without oscillations, which this paragraph elucidates.

Persson and Peraire introduced a shock-capturing approach for high-order discontinuous Galerkin methods, which can stabilise the solution at the sub-cell level. They also developed a reliable shock-detection sensor to complement this stabilisation strategy [25]. Barter and Darmofal proposed an extension to this method in which the element-wise constant artificial viscosity was replaced with a PDE-based formulation. This modification enabled smoother variation of artificial viscosity and reduced sensitivity to errors on unstructured meshes [26]. Moro et al. presented an alternative method in which the activation of artificial viscosity is triggered by the divergence of the velocity. Their results demonstrated that the approach does not interfere with other flow features and contact discontinuities [27]. Compared with the PDE-based method of Barter and Darmofal, it has the advantage of avoiding the solution of an additional equation and does not impose restrictions on the CFL condition, therefore eliminating the strict requirement for implicit integration in Persson and Peraire [27]. All of the approaches are valuable, and some may even offer greater stability, but ultimately Nektar++ adopts the technique proposed by Persson and Peraire for its robustness and wide validation [28].

To sum up, the literature review highlights three key points. Firstly, LPTs are central to modern propulsion systems, with high-speed variants such as SPLEEN remaining relatively unexplored. Secondly, higher-order CFD methods, including Nektar++, have demonstrated strong potential for turbomachinery applications but validation has so far focused on incompressible solvers and canonical cascades. Lastly, stabilisation strategies, particularly artificial viscosity, are essential for capturing shocks in compressible flows. This study addresses these gaps - we follow the simulation setup from Borbouse et al. We explain the numerical methods relevant to Nektar++, including their mathematical formulation, implementation and treatment of boundary conditions. Then, we present the SPLEEN cascade results, evaluate them against existing data and provide insights into Nektar++ compressible-flow solver and artificial viscosity capabilities. Finally, we conclude by outlining the directions for future turbomachinery studies.

2.4 Project Aim and Objectives

The aim of the project is to evaluate accuracy, robustness and best-practice guidelines for using the Nektar++ compressible-flow solver on the SPLEEN LPT. The solver's performance will be assessed through comparison with experimental data and a RANS baseline, with particular focus on the influence of artificial viscosity in high-order discretisation.

1. Review high-order CFD studies of LPT cascades and SPLEEN experiments; define target validation metrics.
2. Develop a Star-CCM+ RANS baseline model for initialisation and reference.
3. Set up dimensional and non-dimensional 2D Nektar++ simulations at Mach 0.7, 0.9 and 0.95; calibrate solver parameters (e.g. Δt , polynomial order, and artificial viscosity coefficients) for stable convergence.
4. Assess Nektar++ predictions against SPLEEN experimental data across defined metrics.
5. Quantify impact of artificial viscosity on result smoothness, resolution and accuracy.

3 Numerical Methods

3.1 Spectral/hp element method

Spectral/hp element methods represent a modern alternative to conventional CFD approaches. While traditional solvers typically achieve accuracy by refining the mesh to a very fine resolution, spectral/hp element methods increase accuracy through high-order polynomial expansions within each element. This allows high-fidelity results to be obtained on relatively coarse meshes, by combining mesh subdivision (*h*-refinement) with polynomial order increase (*P*-refinement). This way Nektar++ exploits the accuracy of spectral methods together with the geometric flexibility of the finite element method [29]. The following paragraph explains the theoretical building blocks of the compressible solver implemented in Nektar++ framework taken from [30].

To illustrate the method consider the linear advection equation, given by:

$$\frac{\partial u}{\partial t} + a \frac{\partial u}{\partial x} = 0, \quad (1)$$

which models transport of a scalar u with speed a . The domain is divided into non-overlapping elements, and within each element the solution is approximated by a polynomial of order P :

$$u^\delta(x) \approx \sum_{i=0}^P \hat{u}_i \phi_i(x), \quad (2)$$

where ϕ_i are basis functions (for example Lagrange or Legendre polynomials) and \hat{u}_i are the corresponding coefficients. Increasing the polynomial order allows representation of progressively

finer flow features without requiring excessively refined meshes. Since u^δ is only an approximation, substituting it into the governing equation produces a residual. To obtain a solvable system, the equation is multiplied by test functions (weight) and integrated over the domain, leading to the weak Galerkin form in which the resulting weighted residual equation is set to zero. In the Galerkin method, the test functions are chosen from the same basis $\phi_i(x)$ as the expansion function $u^\delta(x)$. The semi-discrete system can be written in the following form:

$$\sum_e \left(\phi, \frac{\partial u}{\partial t} + \nabla \cdot F(u) \right)_{\Omega_e} = 0, \quad (3)$$

where $(\cdot, \cdot)_{\Omega_e}$ denotes the element-wise integration over domain Ω_e and subscripts were dropped for simplicity. At this point it is important to emphasise that the compressible solver in Nektar++ uses the discontinuous Galerkin (DG) method. Unlike continuous Galerkin approaches, the DG formulation allows the solution to be discontinuous across element interfaces. This provides flexibility but also introduces a key challenge – information must still be able to propagate between elements. The neighbouring elements are coupled through numerical fluxes, which arise naturally from double integration by parts of Equation 3. The DG formulation in an element can be written as the original conservation law plus a correction for fluxes:

$$\sum_e \left(\phi, \frac{\partial u}{\partial t} + \nabla \cdot F(u) \right)_{\Omega^e} + \langle \phi (\hat{F}(u) - F(u^e)) \cdot n \rangle_{\partial \Omega^e} = 0, \quad (4)$$

where $\langle \cdot \rangle_{\partial \Omega^e}$ represents integration over the element boundary $\partial \Omega^e$ and $\hat{F}(u)$ is the numerical flux. In compact form, this is given by:

$$\text{conservation law} + (\text{interface flux} - \text{element flux}) = 0.$$

Since each element is solved independently, boundary conditions must be imposed at the interfaces (blue lines in Figure 2a). This coupling is achieved through the numerical flux, which enforces the appropriate upwind properties. For example, in Figure 2b, if the velocity V is positive, the upwind direction lies on the left-hand side, so the interface flux is taken as $F(u^3)$.

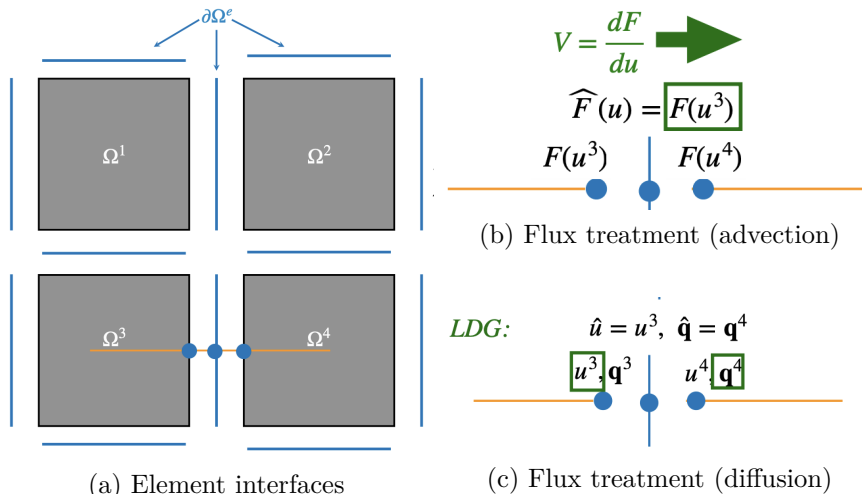


Figure 2: Discontinuous Galerkin interface treatment from [30].

It is also important to consider how the diffusion part of Navier-Stokes equations is dealt with in spectral/hp element methods, which describes the tendency of a property u to spread from high to low concentration regions. The diffusion equation is expressed as:

$$\frac{\partial u}{\partial t} = \mu \nabla^2 u, \quad (5)$$

where μ denotes the diffusion coefficient, which governs the rate of the spreading process. To simplify the second-order partial differential equation (PDE), an auxiliary variable is introduced such that $q = \nabla u$. This transformation reduces the problem to a system of first-order PDEs, though with twice as many equations. The weak formulation is then derived, leading to a problem structure similar to that of the advection operator, in which the treatment of boundary conditions between elements must again be addressed. Unlike advection, the diffusion operator does not have directionality and instead propagates in all directions uniformly. To define numerical fluxes, several approaches can be used, such as the local discontinuous Galerkin (LDG) scheme, in which the variable u is taken from one side of the interface, while q is taken from the other side – see Figure 2c. While LDG illustrates the concept clearly, in this work the diffusion operator is treated using the slightly less intuitive symmetric interior penalty Galerkin (SIPG) method, which retains the second-order form and enforces continuity by adding a penalty term proportional to the jump across element interfaces [31].

Once the governing equations are formulated, they must be solved numerically. An implicit approach is adopted to avoid the severe stability restrictions of explicit schemes at higher polynomials, where the timestep scales as $O(P^{-2})$ for advection and $O(P^{-4})$ for diffusion [30]. Numerical differentiation is carried out by approximating the solution with polynomial basis functions (e.g. Lagrange or Legendre polynomials) and differentiating these expansions, while integration is performed using Gauss-Lobatto-Legendre quadrature. This ensures exact evaluation of polynomial terms up to order $2P - 3$ and plays a key role in controlling aliasing errors arising from non-linear terms. The solution is obtained using the Jacobian-Free Newton-Krylov method – Newton method is used to linearise the initially non-linear system and the GMRES algorithm solves the system, employing pre-conditioning to speed up convergence – the implementation details in Nektar++ can be found in [31].

In summary, this section outlined the implementation of spectral/hp element methods relevant to the compressible solver in Nektar++. A central aspect of the discontinuous Galerkin method is the treatment of advection and diffusion operators, which require the definition of numerical fluxes across element interfaces to maintain stability and consistency. The specific solver settings employed in this study are described in Section 4.3.

3.2 Governing Equations

The fluid flow around the turbine blade is characterised by two-dimensional compressible Navier-Stokes equations [28 and 29]:

$$\frac{\partial \mathbf{q}}{\partial t} + \frac{\partial \mathbf{f}}{\partial x} + \frac{\partial \mathbf{g}}{\partial y} = 0, \quad (6)$$

where $\mathbf{q} = (\rho, \rho u, \rho v, E)^T$ is the vector of conserved variables, ρ is the density, u, v are the velocity components in x- and y-directions, respectively, and E is the total energy, which is related to pressure p as follows:

$$E = \frac{p}{\gamma - 1} + \frac{1}{2} \rho (u^2 + v^2), \quad (7)$$

where γ is the ratio of specific heats. Vectors of fluxes $\mathbf{f} = \mathbf{f}(\mathbf{q}, \nabla(\mathbf{q}))$, $\mathbf{g} = \mathbf{g}(\mathbf{q}, \nabla(\mathbf{q}))$ depend on both the variables as well as their gradients, and can be written as the difference between relevant inviscid ($\mathbf{f}_i, \mathbf{g}_i$) and viscous fluxes ($\mathbf{f}_v, \mathbf{g}_v$):

$$\mathbf{f} = \mathbf{f}_i - \mathbf{f}_v, \quad \mathbf{g} = \mathbf{g}_i - \mathbf{g}_v,$$

where the inviscid fluxes are written as:

$$\mathbf{f}_i = \begin{Bmatrix} \rho u \\ p + \rho u^2 \\ \rho u v \\ u(E + p) \end{Bmatrix}, \quad \mathbf{g}_i = \begin{Bmatrix} \rho v \\ \rho u v \\ p + \rho v^2 \\ v(E + p) \end{Bmatrix}$$

and viscous fluxes are expressed by:

$$\mathbf{f}_v = \begin{Bmatrix} 0 \\ \tau_{xx} \\ \tau_{yx} \\ u \tau_{xx} + v \tau_{yx} + k T_x \end{Bmatrix}, \quad \mathbf{g}_v = \begin{Bmatrix} 0 \\ \tau_{xy} \\ \tau_{yy} \\ u \tau_{xy} + v \tau_{yy} + k T_y \end{Bmatrix},$$

where $\tau_{xx}, \tau_{yy}, \tau_{xy}, \tau_{yx}$ are components of the 2D stress tensor ¹:

$$\begin{aligned} \tau_{xx} &= 2\mu \left(u_x - \frac{u_x + v_y}{3} \right), \\ \tau_{yy} &= 2\mu \left(v_y - \frac{u_x + v_y}{3} \right), \\ \tau_{xy} &= \tau_{yx} = \mu (v_x + u_y), \end{aligned}$$

with k being the thermal conductivity and μ as dynamic viscosity. The Navier-Stokes equations are mathematically analogous to the advection-diffusion forms introduced earlier, enabling the same approach to be applied to obtain the numerical solution.

¹The subscripts denote partial derivatives with respect to that variable, e.g. $u_x = \frac{\partial u}{\partial x}$

3.3 Non-dimensionalisation Strategy

The RANS results from Star-CCM+ will be used as the initial condition for the Nektar++ solver. Since one of the objectives of the project is to compare the dimensional and non-dimensional Nektar++ setup, the dimensional output from Star-CCM+ must be appropriately non-dimensionalised. This subsection describes the non-dimensionalisation strategy employed in this project, which ensures consistency between solvers and additionally reduces the number of independent physical parameters.

One standard way of non-dimensionalisation is to define reference quantities for length, density, temperature and velocity. For turbomachinery applications, blade chord-length is typically chosen as the reference quantity [4]. It is important to highlight that true chord was used, not axial, as this choice ensures better representation of pressure behaviour in turbine blade simulations [32]. The remaining reference values – ρ_∞ , T_∞ and u_∞ – are sampled at the boundary inlet. This location ensures that the reference values are independent of boundary layers or local flow acceleration near the blade. In this project, multiple simulation scenarios were run and non-dimensionalisation was performed individually for each case.

The following relations show how non-dimensionalisation was performed for relevant quantities, where superscript asterisk * indicates non-dimensional quantities:

$$\begin{aligned} L^* &= \frac{L}{c}, & t^* &= \frac{t u_\infty}{c}, \\ T^* &= \frac{T}{T_\infty}, & \rho^* &= \frac{\rho}{\rho_\infty}, \\ u^* &= \frac{u}{u_\infty}, & R^* &= \frac{RT_\infty}{u_\infty^2}. \end{aligned}$$

Nektar++ also requires extra dimensionless quantities to be defined. For this case, that is Reynolds and Mach numbers, given by expressions:

$$Re = \frac{\rho_\infty u_\infty c}{\mu_\infty}, \quad M = \frac{u_\infty}{a_\infty},$$

where μ_∞ is the freestream dynamic viscosity, R is the specific gas constant [4] and the speed of sound $a_\infty = \sqrt{\gamma RT_\infty}$.

3.4 Artificial Viscosity

The SPLEEN cascade investigated in this study is a high-speed LPT, where the presence of shocks in the flow is expected. These abrupt changes in density pose a significant challenge for numerical simulations, often giving rise to Gibbs-type oscillations and potential numerical instabilities [25]. To mitigate these issues, shock detection and capturing methods should be employed. While there are multiple approaches to shock capturing (see Section 2.3), Nektar++

implements the technique proposed by Persson and Peraire, which is detailed below. This method quantifies solution smoothness using a sensor and applies localised artificial viscosity to the governing equations, effectively damping the numerical fluctuations [28]. The modal sensor (or smoothness indicator as referred to by Persson and Peraire) is given by:

$$s_e = \log_{10} \left(\frac{\langle q - \tilde{q}, q - \tilde{q} \rangle}{\langle q, q \rangle} \right), \quad (8)$$

where $\langle \cdot, \cdot \rangle$ represents the standard inner product in L^2 space, and q and \tilde{q} are full and truncated representations of a variable. In the case of Nektar++ the variable is density [28]. Note that the full and truncated solutions are given, respectively, by:

$$q(x) = \sum_{i=1}^{N(P)} \hat{q}_i \phi_i, \quad \tilde{q}(x) = \sum_{i=1}^{N(P-1)} \hat{q}_i \phi_i,$$

where $N(P)$ is the total number of terms in the expansion [25]. The constant element-wise sensor is given by:

$$S_\varepsilon = \begin{cases} 0 & \text{if } s_e < s_0 - \kappa \\ \frac{1}{2} \left(1 + \sin \frac{\pi(s_e - s_0)}{2\kappa} \right) & \text{if } |s_e - s_0| \leq \kappa \\ 1 & \text{if } s_e > s_0 + \kappa \end{cases}$$

where $s_0 = s_\kappa - 4.25 \log_{10}(P)$ [28]. Variables s_κ and κ control the threshold and sharpness of artificial viscosity activation, respectively. Finally, artificial viscosity is formulated by the following equation, where ε_0 controls the magnitude of added artificial diffusion (note that in Nektar++ the parameter is called `mu0`):

$$\varepsilon = \varepsilon_0 \frac{h}{P} \lambda_{\max} S_\varepsilon, \quad (9)$$

where λ_{\max} is the maximum wave speed of the system. To summarise, s_e calculates the smoothness of the solution, based on which the sensor S_ε activates and scales the magnitude of artificial viscosity. When triggered, this adds a Laplacian term to the governing equations (Eq. 6) to dampen the numerical fluctuations locally.

4 Problem Formulation

4.1 Domain Geometry and Mesh

SPLEEN cascade has been previously studied both experimentally [23, 24], and numerically [7, 21, 22]. The geometry is presented in Figure 3. The inlet and outlet boundaries are placed sufficiently far to minimise the influence of boundary conditions on the solution (Figure 4); the inlet is located $2 \times c$ upstream of leading edge (LE), and the outlet $2.4 \times c$ downstream of the trailing edge (TE). The origin of the coordinate system is placed at the LE.

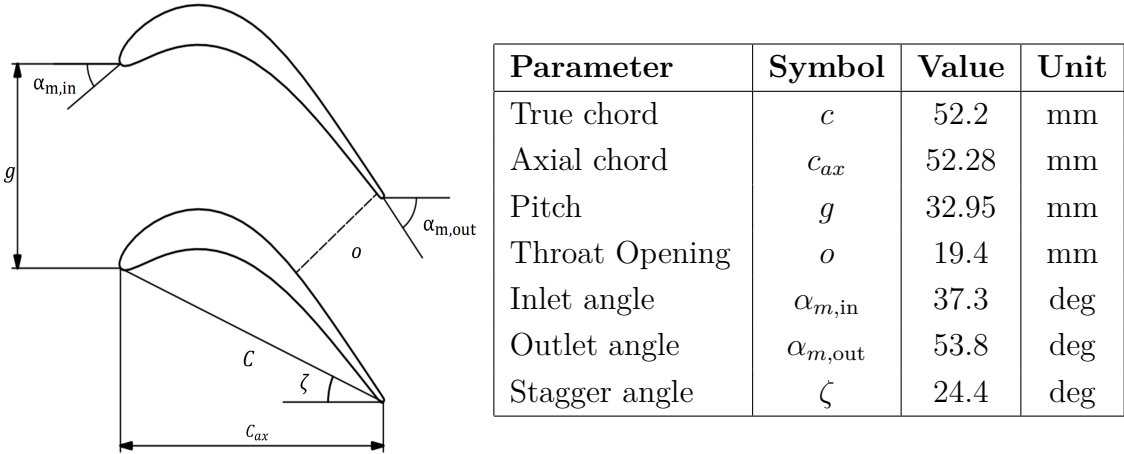


Figure 3: Blade geometry illustration from [33] and corresponding parameters from [7].

The computational domain was generated and meshed in 2D using Gmsh [34] with a third-order mesh, where curved boundaries (such as the blade surface) are represented using cubic polynomial mappings, ensuring accurate geometry approximation consistent with the high-order discretisation. The mesh uses 8860 quadrilateral elements. Near the blade, wall-normal direction is 0.02% of c and wall-tangential is 1% of c to resolve steep gradients. Additional refinement was applied at LE and TE to improve resolution in these regions – see orange boxes in Figure 4. The surrounding blade vicinity is refined to $\sim 4\%$ of c to capture potential shocks and turbulent flow (green box in Figure 4). The boundary layer uses a growth ratio of 1.2 with a total thickness of 2% of c , ensuring smooth expansion away from the wall. Regions far from the blade are deliberately coarser to reduce computational cost where the flow

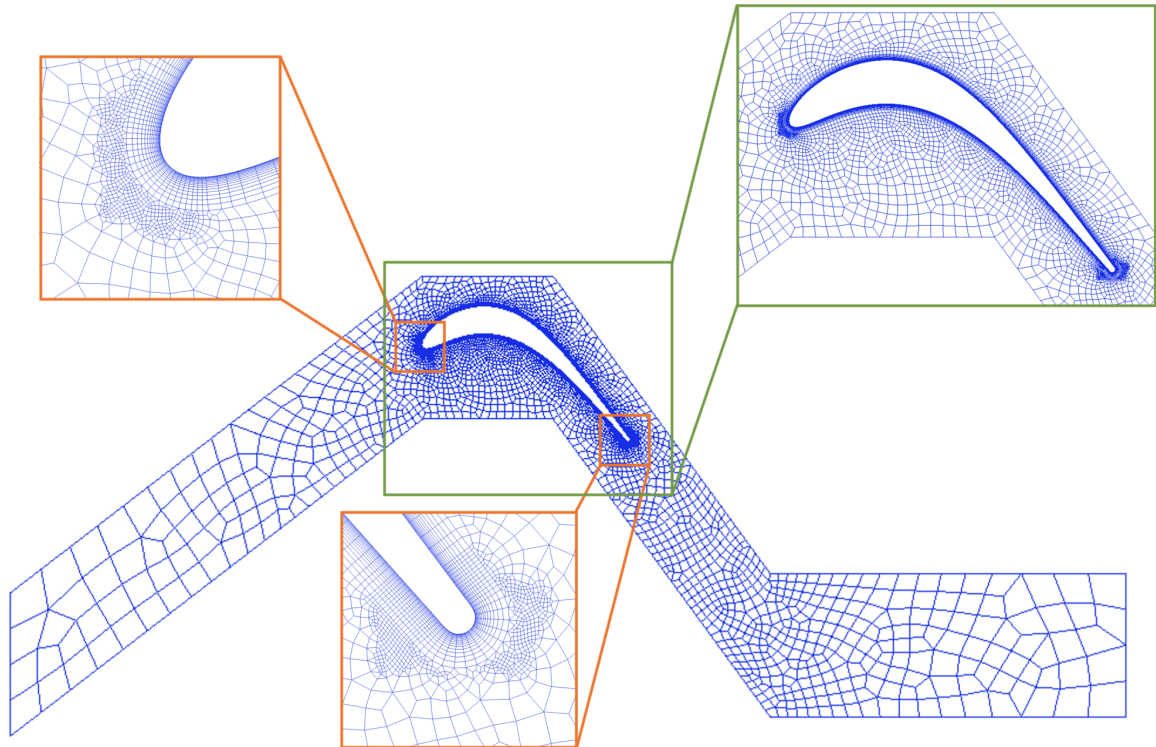


Figure 4: Computational domain and mesh with zoom on refinement regions.

is less critical. Sponge layer for damping numerical pressure waves was not included to avoid additional setup complexity, though adding one later would likely help with acoustic reflections.

Since this study is concerned with accurate numerical modelling, it is vital to study the spatial resolution in wall tangential (Δx^+) and normal (Δy_{wall}^+) directions and ensure it's in the appropriate range. Note that for high-order discretisation, the expression for wall resolutions involves the target polynomial order. The following equations describe a quantitative way of assessing mesh resolution [35]:

$$\Delta x^+ = \frac{\Delta x u_*}{P\nu}, \quad \Delta y_{wall}^+ = \frac{\Delta y u_*}{P\nu}$$

where P is the solution polynomial order, $u_* = \sqrt{\tau/\rho}$ is the friction velocity, τ is the wall-shear stress magnitude, ρ is the density, ν is the kinematic viscosity and Δx , Δy are mesh spacing in tangential and normal directions, respectively. The wall resolution assessment criteria suggested by Georgiadis et al. have been used (Table 1), as it is an established measure of estimating the resolution of the near-wall mesh.

Table 1: Typical near-wall grid spacing requirements for LES and DNS from [36].

	LES	DNS
Δx^+	< 50	< 10
Δy_{wall}^+	< 1	< 1

As shown in Figure 5, the near-wall mesh meets DNS quality criteria, indicating that the simulation adequately resolves the flow in this critical region. For the highest polynomial ($P = 4$), the wall-tangential spacing satisfies $\Delta x^+ < 6$ and the wall-normal spacing remains below $\Delta y_{wall}^+ < 0.6$, both consistent with DNS requirements presented in Table 1. Even the second-order mesh ($P = 2$) meets these criteria, confirming that the current third-order mesh is well suited to the simulation objectives.

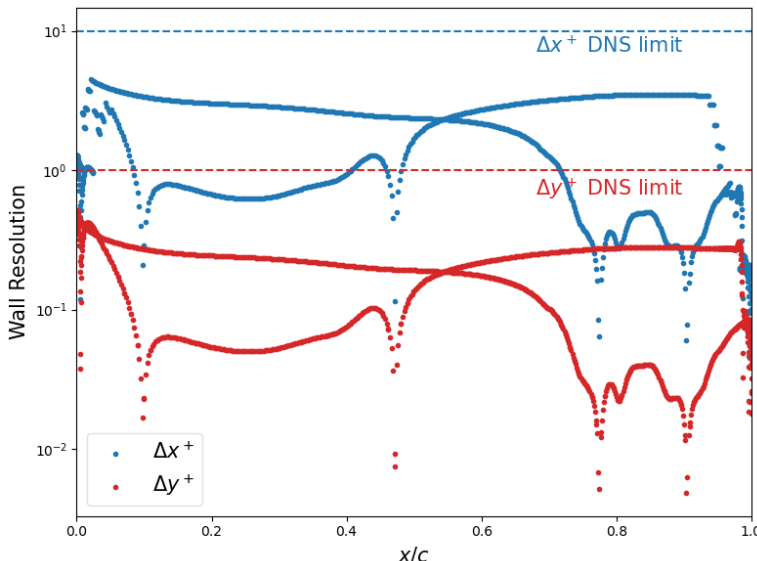


Figure 5: Near-wall resolution ($P = 4$).

4.2 Parameters and Boundary Conditions

The working fluid is modelled as an ideal gas with a specific heat ratio of $\gamma = 1.4$, Prandtl number of $Pr = 0.72$ and gas constant $R = 287.058 \text{ Jkg}^{-1}\text{K}^{-1}$ and viscosity calculated using Sutherland's law [7]. Simulations were carried out for three outlet Mach numbers: $M_{out} = 0.7, 0.9, 0.95$. A uniform non-dimensional timestep of $\Delta t = 5 \times 10^{-4}$ was used, with appropriate dimensionalisation applied for dimensional runs. At the inlet, static Dirichlet conditions are prescribed for the conservative variables ($\rho, \rho u, \rho v, E$). At the outlet, a subsonic pressure-outlet is imposed. The blade surface is modelled as a no-slip adiabatic wall. The pitchwise boundaries are periodic. No inflow turbulence was injected. The reference length is the true chord c and all remaining quantities are derived from Table 2. These values originate from RANS results obtained with Star-CCM+, providing suitable initial conditions for Nektar++. AV was applied where necessary to stabilise shocks.

In Table 2 the Mach and Reynolds numbers are labelled "target" because the outlet values cannot be prescribed directly; they were computed a posteriori from the time-averaged solution as a sanity check.

Table 2: Simulation parameters for three cases.

Parameter	Symbol	Value			Units
Outlet static pressure	p_{out}	7771.16	5617.12	5213.22	Pa
Inlet static temperature	T_∞	288.54	286.88	286.866	K
Inlet density	ρ_∞	0.1136	0.0987	0.0968	kg/m^3
Inlet Mach number	M_{in}	0.445	0.478	0.478	-
Inlet Reynolds number	Re_{in}	50304	47556	46062	-
Target Mach number	M_{out}	0.7	0.9	0.95	-
Target Reynolds number	Re_{out}		70000		-
Flow angle	α		37.3		deg

4.3 Solver Configuration

This study solves the compressible Navier-Stokes equations using discontinuous Galerkin method. Both advection and diffusion are solved implicitly using a second-order Singly Diagonally Implicit Runge-Kutta scheme (DIRK2). The Roe approximate Riemann solver is used to handle the discontinuities between elements. Standard DG operators are chosen for advection and diffusion – classical DG in weak form and symmetric interior penalty method, respectively. All parameters are listed in Table 4 in the Appendix.

Aliasing errors may be introduced when non-linear terms are evaluated at an insufficient number of quadrature points, which could lead to instabilities in the simulation [28]. To mitigate

this issue, a larger number of quadrature points is employed so that all non-linear contributions arising in simulations are consistently integrated. The number of quadrature points was calculated using:

$$Q = P_{\text{exp}} + \frac{P_{\text{exp}} + 3}{2} \quad (10)$$

where P_{exp} is the polynomial expansion order. Note that the expression was adjusted from [28].

4.4 Conservative Variables

Compressible solver uses the conservative variables, unlike the incompressible solver which uses the primitive variables (u, v, p). Variables u, v were multiplied by respective ρ values to obtain $\rho u, \rho v$ and ρ, E are left unchanged. This way all variables are represented in conservative form – $\rho, \rho u, \rho v, E$. It is important to note that for the dimensionless case, the values are first non-dimensionalised, then converted to conservative.

4.5 Convergence and Time Averaging

Traditional CFD solvers assess convergence by monitoring residuals, which indicate the imbalance between the right- and left-hand sides of the governing equations. When these values are sufficiently small, the solution is considered converged to a steady state. In contrast, spectral/hp element methods target unsteady flows, replacing the conventional approach with statistical analysis; the temporal evolution of a chosen quantity (e.g. modal energy, $c_{l/d}$, time-averaged flow fields) is monitored until its average reaches a stable plateau. This section presents the procedure to determine statistical convergence of a Nektar++ simulation.

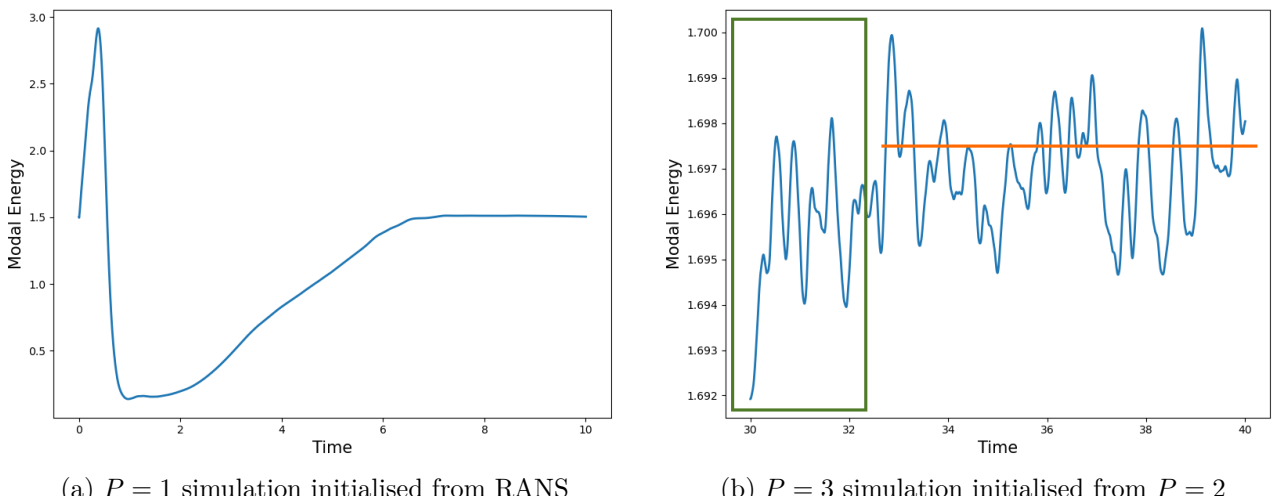


Figure 6: Statistical convergence assessment. *Time* denotes convective time units (CTU).

Figure 6a shows the temporal evolution of the modal energy for the $P = 1$ simulation, initialised from a steady-state RANS solution obtained with Star-CCM+. The initial transient phase is clearly visible, with the modal energy undergoing large changes before stabilising to an

approximately constant value after around $CTU \approx 7$. This indicates that the transient effects in the modal energy have dissipated, and the flow has reached a statistically stationary condition. Figure 6b presents the modal energy for the $P = 3$ simulation, which was initialised from a $P = 2$ solution (itself initialised from $P = 1$). This case is plotted 30 time units later than Figure 6a, and uses a different (zoomed-in) vertical scale, making the fluctuations appear larger than they are. The green box marks the estimated transient period, after which the solution oscillates around a mean value, shown by the orange line. This mean was determined empirically from the data. Such oscillatory behaviour is expected, as real turbulent flows are inherently unsteady, and thus the modal energy will never be perfectly constant. The observed plateau in the mean confirms that the simulation duration was appropriate. This type of analysis was performed for every simulation to ensure statistically steady behaviour.

4.6 Simulation Workflow

The objectives of the report were achieved by running numerical simulations according to the following workflow. First, the problem was implemented in Star-CCM+, which is shown in Appendix D, since the RANS simulations only served as a benchmark for high-fidelity Nektar++ studies. Then, Nektar++ solver was used to simulate the flow, starting from low polynomial order ($P = 1$), which was incrementally increased to ensure numerical stability until $P = 4$. The parameters in the setup file were non-dimensionalised using appropriate reference quantities (see Section 3.3). Additional studies were run with dimensional parameters in the setup file, which were used to compare whether the setup change would create any differences in the final solution; these are elaborated on in Section 5.3. Data post-processing was performed using Python scripts and all flow visualisations were created in Paraview.

It is important to note that, to the best of the author's knowledge, no previous studies have compared dimensional and non-dimensional formulations within Nektar++. This dual-setup strategy therefore constitutes a novel methodological contribution of the present work.

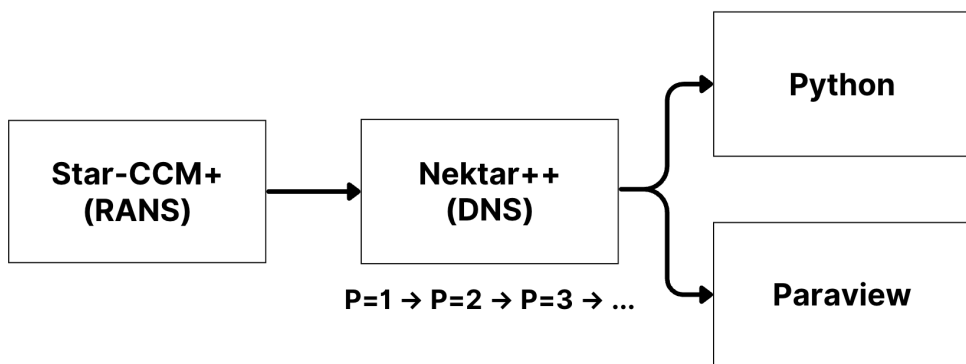


Figure 7: Simulation and post-processing workflow.

5 Results

5.1 Flow Physics

The following sections discuss results obtained from Nektar++ simulations to analyse the flow field and validate the simulations against experimental data from the SPLEEN database [33]. For completeness, a qualitative P -refinement study was conducted to confirm that increasing the polynomial order improves solution accuracy. Since the trends are consistent across all orders, only the highest polynomial results are shown (unless stated otherwise), as they provide the most reliable representation of the flow.

5.1.1 Flow Field Analysis

The analysis begins with a comparison between instantaneous and time-averaged solutions, building on the discussion in Section 4.5. Certain quantities, such as the isentropic Mach number distribution, should be time-averaged to capture the mean behaviour of the flow, ensuring that the graph is representative of the statistically stationary state. Others, however, are best presented instantaneously to study the complex phenomena that are happening at a specific moment. Figure 8 compares instantaneous and time-averaged Mach number fields, illustrating how averaging produces a smoother, dissipative-looking distribution in which essential unsteady features are lost. For instance, Figure 8a shows vortex shedding from the blade, which vanishes in the time-averaged visualisation, leaving a narrow region of reduced velocity in place of vorticity (Figure 8b). Since these structures are inherently unsteady, the averaging process effectively cancels them out. It is therefore crucial to choose carefully between instantaneous or averaged fields to ensure an accurate depiction of the turbine cascade.

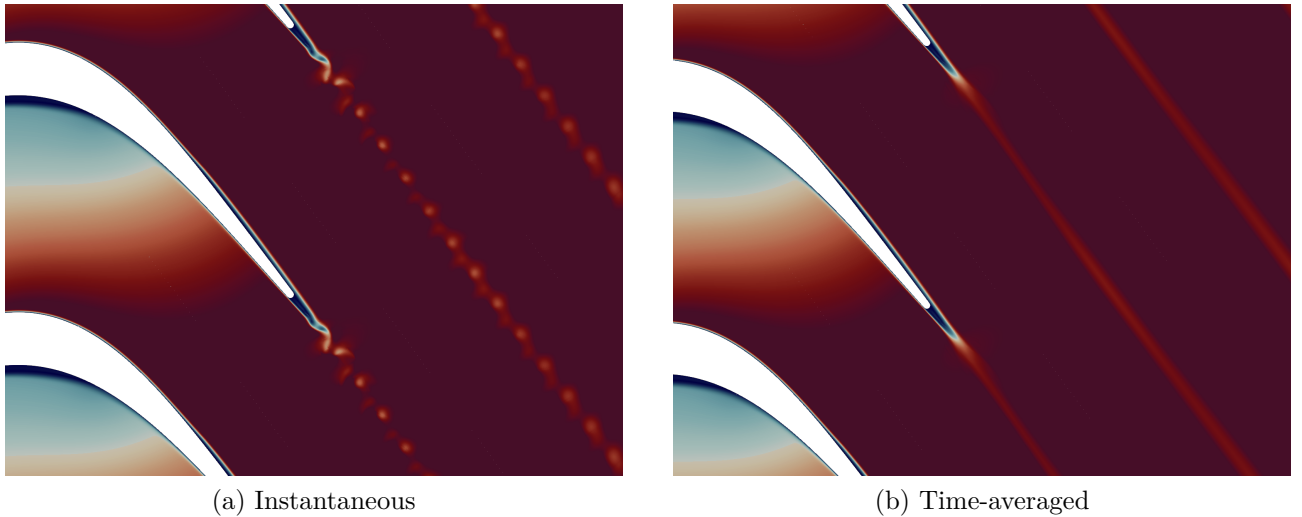


Figure 8: Mach number in the passage.

Having established that instantaneous results should be used for flow-field analysis, the flow behaviour is examined using Mach number contour plots of the turbine passage. These visualisations are used to provide an initial qualitative understanding of the flow physics and to set

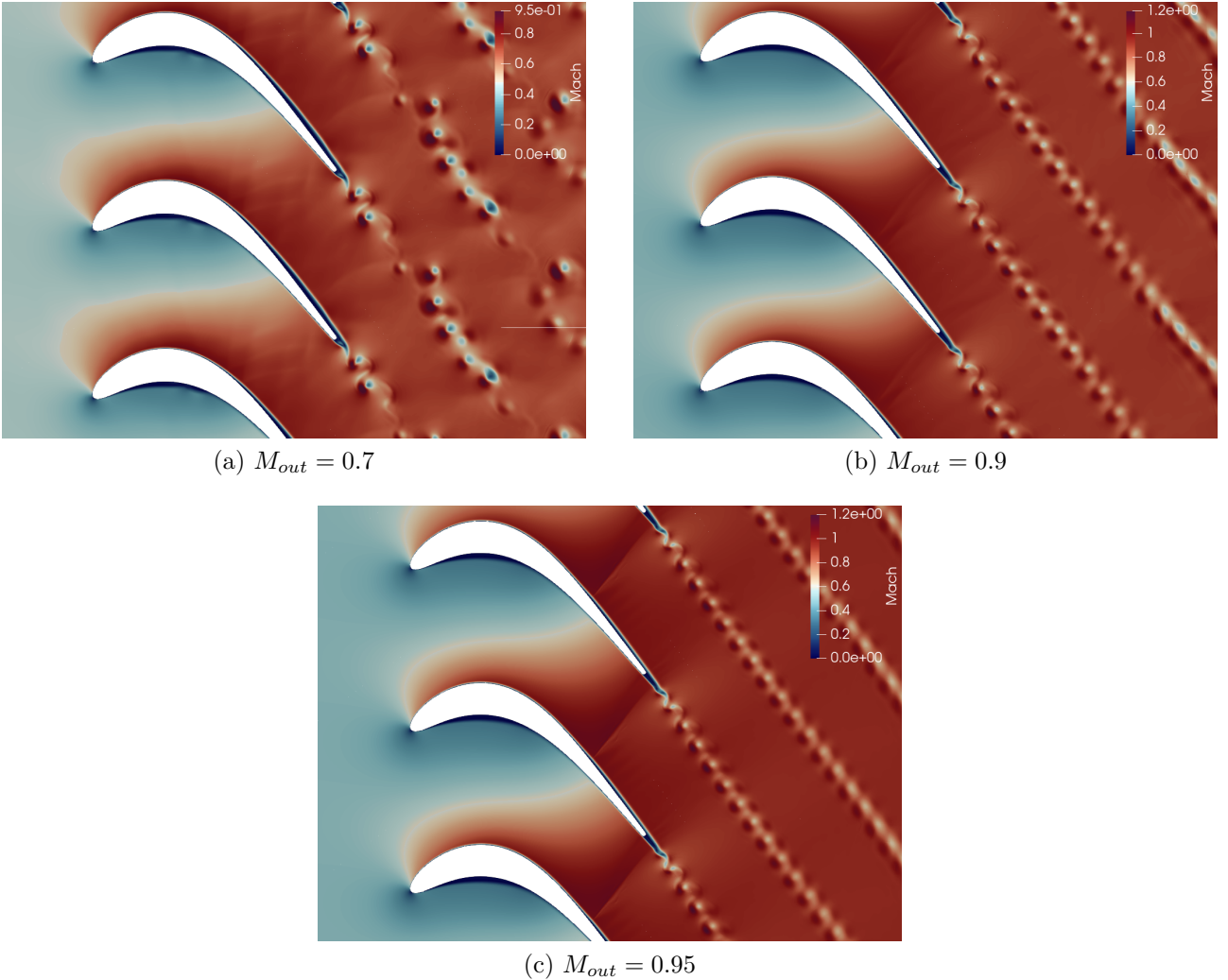


Figure 9: Instantaneous Mach number visualisation after 40 CTUs.

the stage for the quantitative analyses that follow. Note that in all studied cases a separation bubble was observed on the pressure side (dark blue region on the contour plots), which is discussed in detail in Section 5.1.5.

In the subsonic case ($M_{out} = 0.7$), the flow exhibits the typical behaviour; a clear stagnation point forms near the blade LE, and the Mach number on the suction side (SS) is higher than on the pressure side (PS), corresponding to greater velocity – see Figure 9a. The wake is highly perturbed, with vortices shed from the TE in an irregular and non-uniform manner. Their disordered character suggests inherently unstable wake dynamics, leading to increased mixing and therefore higher losses. Additionally, V-shaped acoustic-like perturbations originating at the TE appear between the blades, which are reflected upstream along the blade surface. This behaviour is only observed in the subsonic case, as the presence of shock prevents upstream propagation for the other cases. It is possible that these waves modulate the upstream boundary layer, creating larger turbulent structures that result in a more chaotic wake.

For the $M_{out} = 0.9$ and $M_{out} = 0.95$ cases (Figures 9b and 9c, respectively), the general flow

behaviour (stagnation point location, SS and PS distributions) are also as expected. The passage flow appears cleaner, without the V-shaped 'smears', which is likely due to the presence of transonic or locally supersonic regions. The wake is dominated by a regular oscillatory pattern characteristic of a Kármán vortex street – the wake energy is organised into coherent, periodic vortices, instead of random turbulent structures. The wake also appears narrow, which can be attributed to reduced mixing due to the absence of inflow turbulence in the simulations. Consequently, the predicted losses may not be quantitatively reliable and therefore will not be discussed, especially since turbomachinery flows are inherently three-dimensional and cannot be fully captured in a two-dimensional study. With prescribed inflow turbulence, a broader vortex street would be expected, closer to the physical behaviour.

In both transonic cases, a shock develops between the SS and TE of the neighbouring blade, as shown in Figure 10. This shock suppresses upstream wave propagation from the TE – in contrast to the subsonic case – leading to a cleaner and more regular passage flow. Moreover, in the $M_{out} = 0.95$ case (Figure 10b), a second shock originates at the TE and nearly interacts with the wake of the adjacent blade. This behaviour is characteristic of choked flow, where the throat is located at the TE. The close proximity of the shock to the wake may enhance unsteadiness and contribute to higher losses. This highlights the importance of compressibility effects in HSLPT flows, where strong gradients must be resolved to capture the underlying physics accurately.

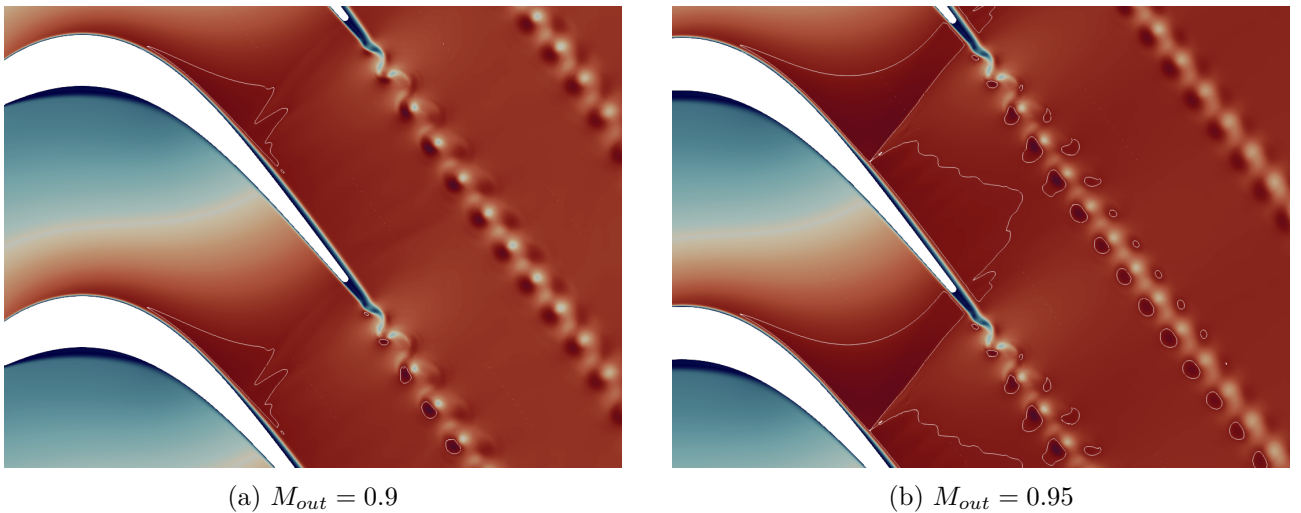


Figure 10: Compressibility effects. White contours correspond to $M = 1$.

5.1.2 Blade Loading

It is common for turbomachinery simulations to discuss the isentropic Mach number, which describes the Mach number that the flow would have if there were no losses in it. Note that all graphs are showing time-averaged isentropic Mach number, where the top graph corresponds to suction surface and the bottom one to pressure surface.

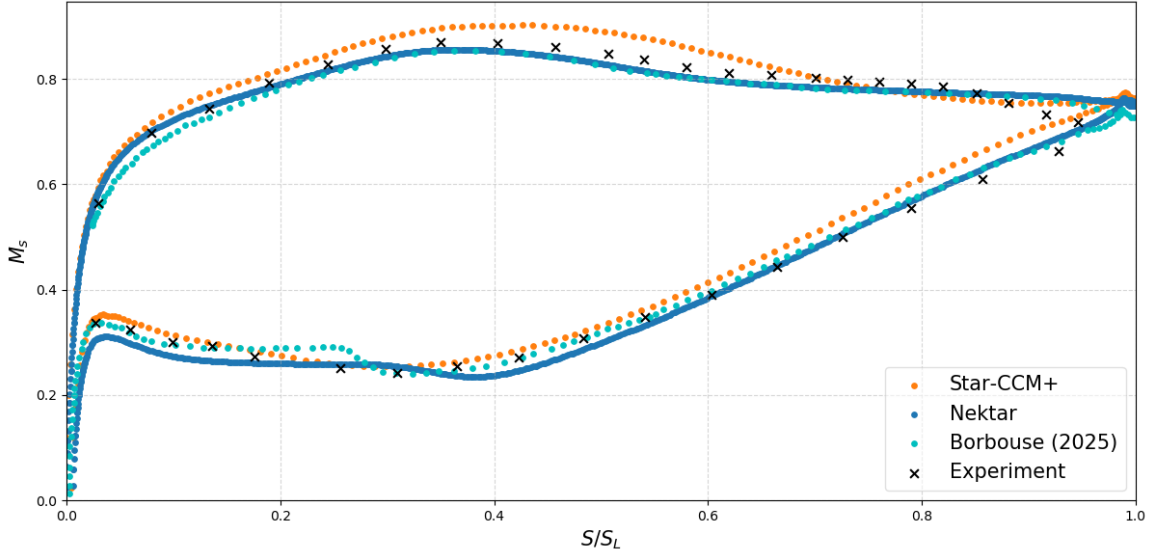


Figure 11: Time-averaged isentropic Mach number ($M_{out} = 0.7$).

Figure 11 presents the time-averaged isentropic Mach number distribution for the subsonic case. On the SS near the LE, Nektar++ reproduces the experimental distribution reasonably well, but several discrepancies arise further downstream. The flow is underestimated on the SS; the aft portion of the blade lacks the pressure recovery observed experimentally, with the characteristic dip in isentropic Mach number entirely absent in the numerical prediction. This plateau in numerical results suggests that the boundary layer (BL) may separate, resulting in a bubble in the aft part of the SS. BL does not transition to turbulent; without inflow turbulence, the flow remains too weak to reattach, which highlights the critical influence of that setup feature, consistent with the prior visualisation studies of Mach number flow fields. Also note that the Star-CCM+ results were not included in the discussion, because generally they show poor agreement with experimental data.

While on the SS, Nektar++ performs comparably to or better than ArgoDG (marked with Borbouse (2025) in the legend), the same cannot be said about the PS. The isentropic Mach number peak near the LE is underpredicted compared with both experimental and ArgoDG results, and the overall distribution is poorly captured. These deviations stem from a numerical bubble forming on the PS, again a consequence of the turbulence-free inflow setting. This bubble alters the pressure field over the majority of the blade surface, leading to significant discrepancies in the predicted isentropic Mach profile. Unlike the transonic cases, where shock dynamics dominate, the purely subsonic flow is controlled almost entirely by BL behaviour and is therefore highly sensitive to inflow turbulence. The influence of the separation bubble is examined in more detail in Section 5.1.5. It was also investigated whether lowering the outlet static pressure influenced the results, but the effect was marginal and lead to an unrealistically high outlet Mach number.

Figure 12 presents the isentropic Mach number distribution for the $M_{out} = 0.9$ case. A key

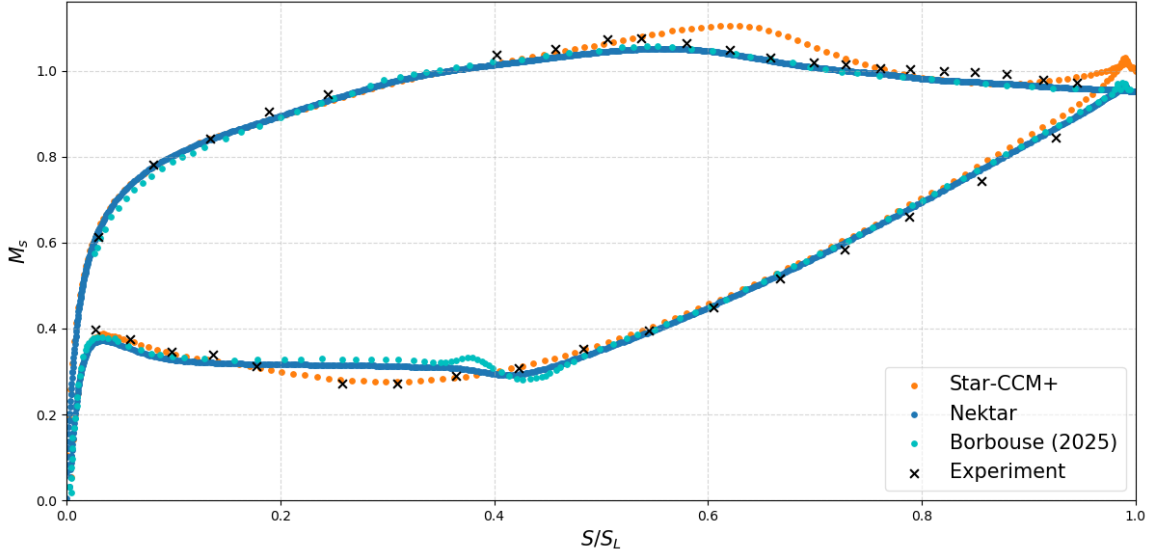


Figure 12: Time-averaged isentropic Mach number ($M_{out} = 0.9$).

observation is that Nektar++ reproduces the experimental data more accurately than Star-CCM+, particularly around the isentropic Mach number peak on the SS ($S/S_L \approx 0.55$), where Star-CCM+ predicts a noticeably stronger peak downstream of the experimental result. Toward the TE, Nektar++ again outperforms Star-CCM+, which tends to overpredict the velocity, distorting the wake characteristics. Although better than RANS, Nektar++ slightly underpredicts the isentropic Mach number of the SS, which could be critical since the aerodynamic force is predominantly generated on the suction surface. In addition, the isentropic Mach number peak is slightly aft of the experimental one, suggesting that the shock (which is downstream of that point) may be also smoothed out. A likely explanation for these discrepancies is the combined effect of numerical dissipation through AV settings (discussed in Section 5.2) and the absence of inflow turbulence. These differences highlight the sensitivity of isentropic Mach number distributions to both inlet turbulence settings and stabilisation choices.

On the other hand, RANS simulations provide a closer match on the PS. Both Nektar++ and ArgoDG results of Borbouse et al. show a long flat region between $S/S_L \approx 0.1$ and 0.35 , suggesting potential separation, which is absent in the wind-tunnel data. Flow-field visualisation confirmed that this feature corresponds to a separation bubble on the PS, likely caused by the absence of inflow turbulence in the high-order simulations, as injected turbulence promotes mixing. Note that the Star-CCM+ simulations included weak inlet turbulence. Refer to Section 5.1.5 for the flow visualisation and a more comprehensive analysis of this numerical phenomenon. Moreover, Nektar++ simulates the isentropic Mach number peak correctly, showing improvement with respect to the subsonic case. Both high-order codes tend to overpredict the isentropic Mach number closer to TE, which is likely a consequence of the numerical bubble.

Lastly, Figure 13 shows the isentropic Mach number distribution around the blade for $M_{out} = 0.95$. The overall trends are consistent with those observed in the previous case. The SS

distribution is very accurate close to the LE and is slightly underpredicted downstream, but generally agrees with both experimental and ArgoDG data.

On the PS, the isentropic Mach number peak is much closer to the experimental data than for the $M_{out} = 0.7$ simulation. The downstream behaviour is similar to the previous transonic case, where a plateau caused by the numerical bubble forms. The distribution in the aft half of the blade shows good agreement with the experimental data. It is important to note that the simulation diverged for $P = 1$ after approximately 4.5 CTUs, roughly when the RANS simulation was flushed away. The run was then finished with $P = 2$, providing additional flexibility required for convergence.

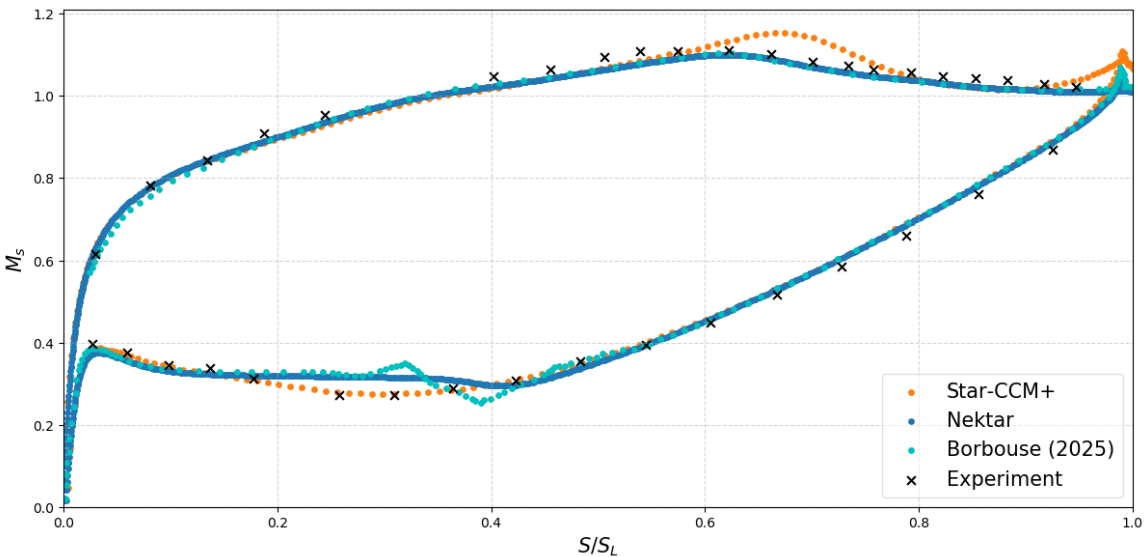


Figure 13: Time-averaged isentropic Mach number ($M_{out} = 0.95$).

5.1.3 Skin Friction

In the analysis of flow, it is also essential to examine the skin friction coefficient, as it provides an indication of the state of the boundary layer, complementing previous observations.

For the pressure side, the variation is consistent across all cases and follows the expected behaviour (Figure 14). A reduction in skin friction downstream of the LE reflects the BL decelerating under the adverse pressure gradient, with separation identified once the coefficient c_f becomes negative. The flow subsequently reattaches, as also observed in the Mach number visualisations (Figure 9), after which the skin friction increases steadily towards the TE. The separation bubble length is found to increase with Mach number, in agreement with ArgoDG results [7]. Notably, for the highest Mach case ($M_{out} = 0.95$), the skin friction peak at the TE is considerably larger than at the LE, which could indicate that BL transitioned to turbulence, however a more in-depth analysis is required to confirm that.

On the suction side, the skin-friction distributions follow a slightly different trend. Although

the initial rise in the friction coefficient near the LE appears in every case, the following pattern in c_f reduction varies. In the subsonic case, the aft section shows clear evidence of separation, as indicated by negative values of c_f between $S/S_L \approx 0.65$ and the TE (Figure 14a). This behaviour is linked to the lower velocity peak in the subsonic case (Figure 11), which leaves the BL with insufficient momentum to overcome the adverse pressure gradient. Importantly, c_f remains negative until the TE, confirming that reattachment does not occur. In the $M_{out} = 0.9$ case, the coefficient becomes momentarily negative around $S/S_L \approx 0.85$, suggesting local separation. Finally, in the highest-speed case, skin friction coefficient decreases towards zero but does not remain clearly negative. While the time-averaged distributions suggest no sustained separation, small regions of transient separation may still appear, with the flow ultimately reattaching before the TE. Notably, the shape of the distributions differs between cases: in the subsonic regime, c_f decreases almost linearly between $S/S_L \approx 0.3$ and 0.6. For the transonic cases, there is a more abrupt change in skin friction coefficient, which is particularly sharp for the $M_{out} = 0.95$ case (Figure 14c). It is speculated that the rapid drop in c_f coincides with the shock location, reflecting the strong interaction between shock dynamics and the BL.

These findings are consistent with the discussion of the passage flow physics and quantitatively support the previous studies. A more detailed investigation of velocity profiles within the BL would provide further insight, but this was not carried out due to time constraints.

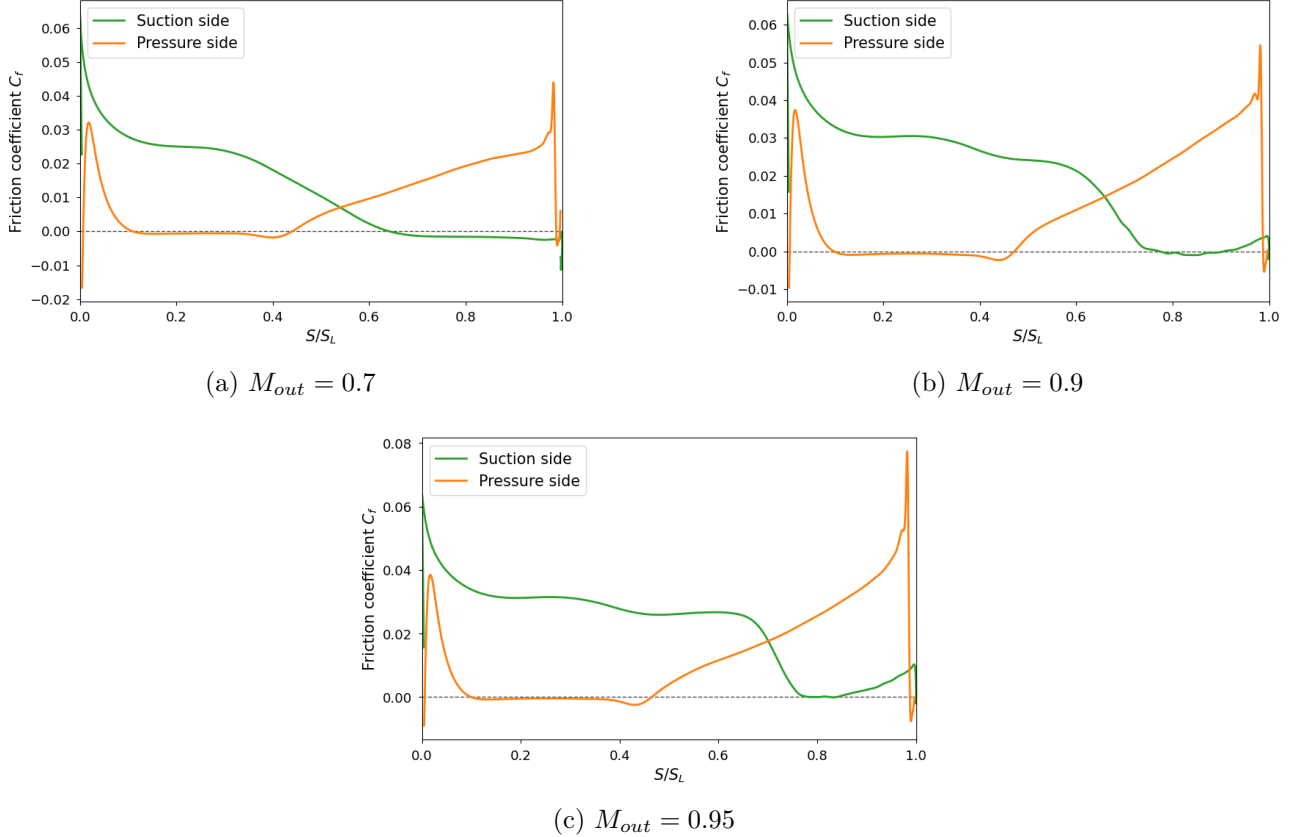


Figure 14: Time-averaged skin-friction coefficient along the blade.

5.1.4 Outlet Mach number

The outlet Mach number was extracted as a validation metric. The results were temporally and spatially averaged, with the mean value used to assess whether the target Mach number was achieved. This step served as a sanity check. The values are not expected to be exact, since the simulations are restricted to two dimensions, and the underlying physics is inherently three-dimensional. As a result, key three-dimensional flow structures (for example vortices) cannot be fully captured, which strongly affects blade and wake loss prediction, leading to inaccuracies in outlet conditions. A 2.5D extrusion would likely improve the accuracy, but even within the 2D framework the results are satisfactory.

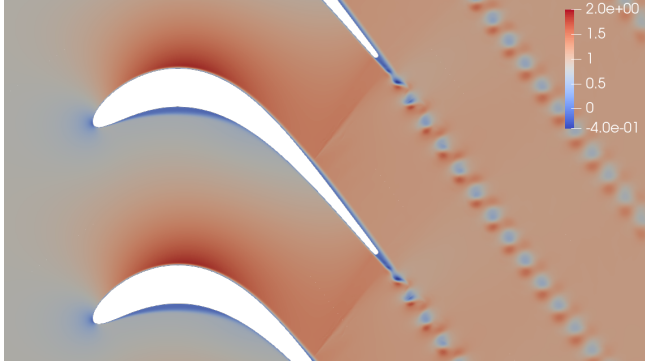
For $M_{out} = 0.7$ results are not shown in Table 3, as the predictions are already very accurate – across all polynomial orders, the deviation from the target value remains below $\pm 1\%$. For $M_{out} = 0.9$ and 0.95 , the error magnitude stays within 3% . A general trend is observed where increasing the polynomial order improves the accuracy of the outlet Mach number prediction, with the exception of the $M_{out} = 0.95$ case when moving from $P = 3$ to $P = 4$. This confirms that, in most cases, the additional computational cost of higher polynomial orders is justified by improved prediction accuracy. It is also important to address the relatively high error for the $M_{out} = 0.95$ case – most likely it is due to three-dimensional flow features emerging at transonic conditions, which cannot be captured in the present two-dimensional setup.

Table 3: Errors in outlet Mach number prediction.

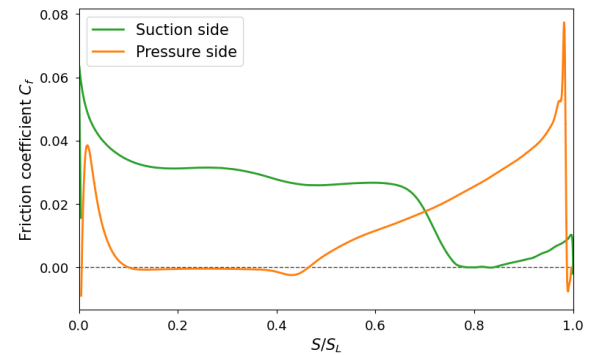
Mach (Target) Polynomial Order	0.9				0.95			
	1	2	3	4	1	2	3	4
Mach (Value)	0.874	0.881	0.885	0.895	0.92	0.927	0.932	0.93
Error, %	-2.9	-2.1	-1.67	-0.5	-3.2	-2.4	-1.8	-2.1

5.1.5 Numerical Bubble

This section analyses the separation bubble observed on the pressure side in the simulations. The streamwise velocity field (Figure 15a) shows a reversed-flow region ($u < 0$, blue) on the pressure surface, consistent with the skin-friction distribution (Figure 15b). Between $S/S_L \approx 0.1$ and 0.35 , c_f becomes negative, indicating that shear stress opposes the mean flow – an attribute of separated flows. The skin friction recovers at $S/S_L \approx 0.45$, suggesting flow reattachment, which is in agreement with velocity field visualisation. Note that these values are for the $M_{out} = 0.95$ case, for the other two the bubble size will vary but the trend is the same. This separation bubble, absent in experimental data, is likely caused by the lack of inflow turbulence; experiments report turbulence intensities of up to $\sim 2.5\%$ [7]. Several papers reviewed in Section 2.2 reported that the inflow turbulence has a profound effect on the simulated flow field [7, 9, 12, 13, 14, 21], which is why it is speculated to be the underlying cause of the numerical bubble. Future work to overcome this obstacle is shown in Section 6.2.



(a) Streamwise velocity field



(b) Friction coefficient variation

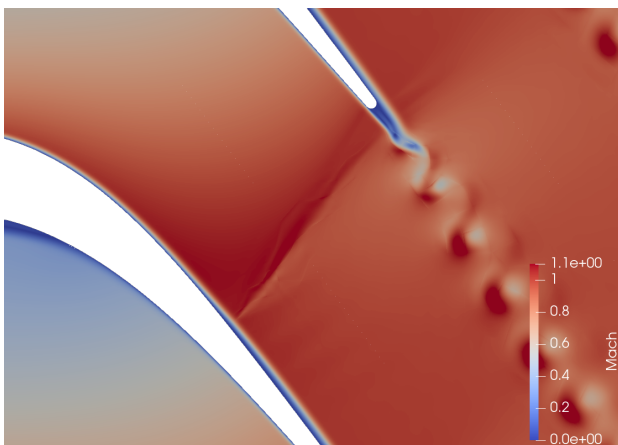
Figure 15: Pressure-surface numerical bubble ($M_{out} = 0.95$, $P = 4$).

5.2 Artificial Viscosity Study

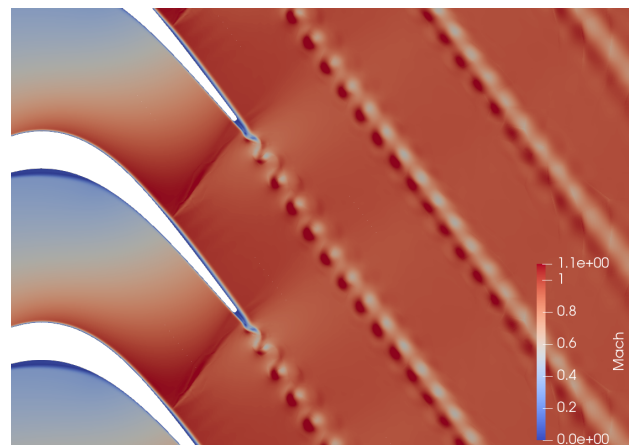
This section examines the artificial viscosity settings with the aim of establishing good practices for their use within the Nektar++ framework. Only results for $M_{out} = 0.95$ are presented, as in the other cases there are no shocks or the shocks are too weak for a meaningful AV analysis.

5.2.1 Finding the Optimum Value

The search for an optimal AV value should begin with the baseline case of zero AV. If the simulation remains stable and delivers satisfactory accuracy, this is the preferred condition, as no additional dissipation is introduced into the governing equations and the flow physics remains unaltered. In the present work, most cases completed successfully without AV. However, the resulting accuracy was insufficient. In particular, the shock was poorly resolved; it should be captured with infinitesimal thickness, which cannot be observed in Figure 16a. The shock looks blurred and under-resolved which suggests that AV should be employed in that case.



(a) Shock resolution



(b) Wake resolution

Figure 16: Key flow features with no AV added.

The second step is to test the case with a high AV value to assess its impact on the flow field. It can be seen that although the shock appears sharper, the wake is highly smoothed (Figure 17).

Excessive AV setting produces a RANS-like wake², which fails to capture the true flow physics, which can be seen in Figure 16b. This effect is highly undesirable and should be avoided – too much AV helps with high gradients but completely distorts the rest of the flow field. It follows that the optimal AV setting should lie between these extremes – sufficiently high to resolve discontinuities locally, yet low enough to avoid unnecessary dissipation in other regions. These results are presented in the next section (Figure 19), since they are also relevant for the polynomial order deliberations.

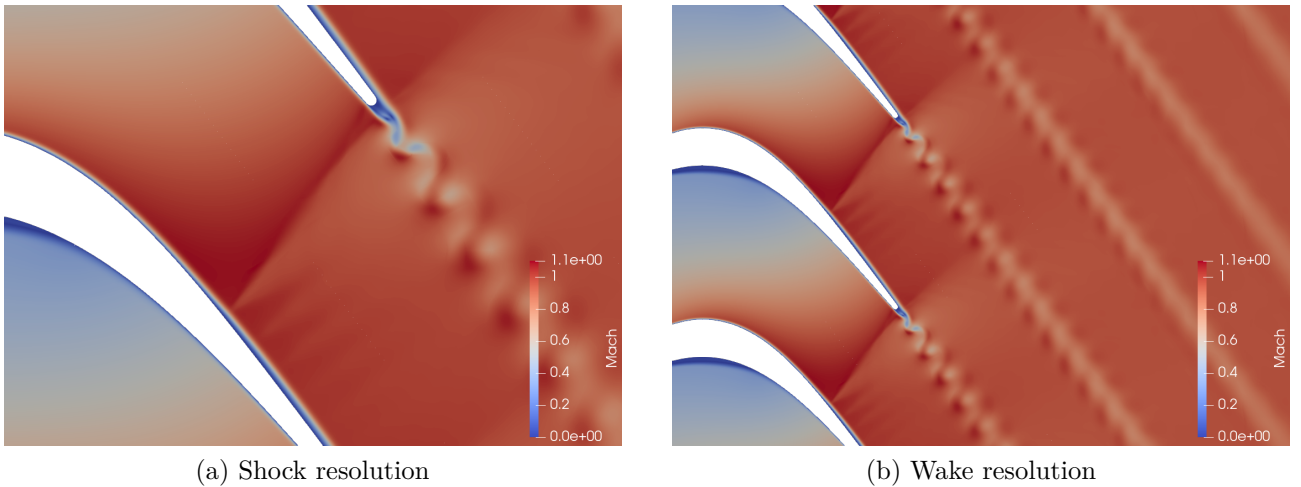


Figure 17: Key flow features with high AV added.

5.2.2 Polynomial Order Influence

This section examines how AV settings should be adapted when varying the polynomial order of the solution. A set of simulations was carried out for $P = 1, 2, 3$ at $M_{out} = 0.95$, using the following baseline parameters: $\mu_0 = 0.01$, $s_\kappa = -1$ and $\kappa = 0.1$. The results in Figure 18 show that, despite identical settings, higher polynomial orders lead to greater AV application. This occurs because the AV activation threshold scales with P – see Section 3.4. As P increases, the threshold decreases, and AV is triggered over a larger portion of the domain. For higher polynomial orders (Figures 18b and 18c) significantly more AV is applied, particularly in the wake, whereas for $P = 1$ (Figure 18a) almost none was added in that region. Additional diffusion also appears around the shock (see orange boxes in Figure 18), which is desirable since a discontinuity is expected there – the shock is under-resolved in Figure 18d and that improves in Figures 18e and 18f. Overall, the comparison confirms that Nektar++ follows the AV formulation of Persson and Peraire as intended.

While in some cases this behaviour can be beneficial, AV should generally be applied with caution. For instance, comparing the Mach number fields for $P = 2$ (Figure 18e) and $P = 3$ (Figure 18f) shows little improvement in wake resolution, even though in principle a higher polynomial should allow for a more detailed representation of the flow on the same mesh. This

²Wake visualisation from RANS simulation is presented in Figure 25 in the Appendix

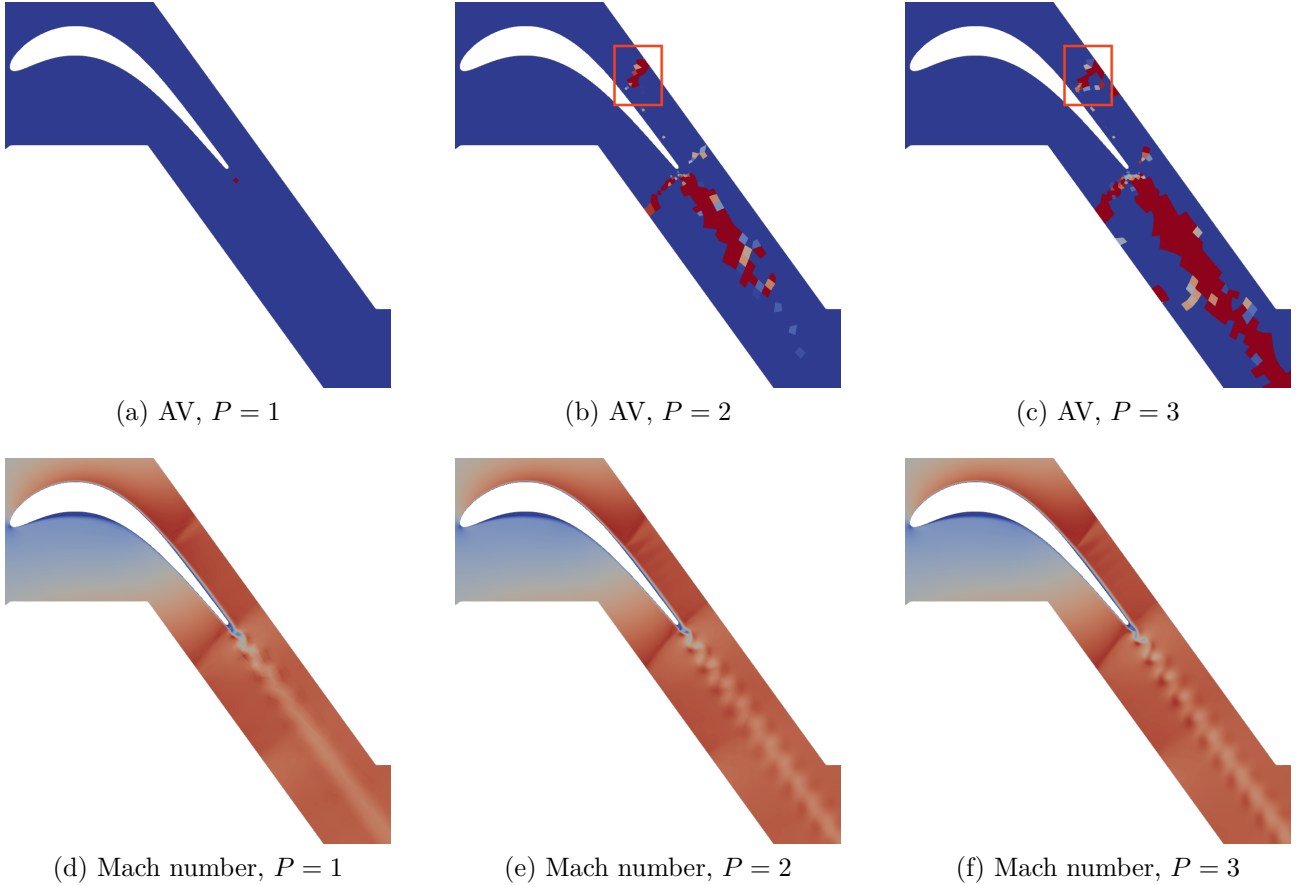


Figure 18: AV result variation with P . Note that AV applied at shock is marked in orange. Results for a single domain are presented for better visibility.

lack of added detail is attributed to AV-induced smoothing. Consequently, AV settings must be carefully tuned to avoid compromising the underlying flow physics.

The following figure presents a case where the AV parameters were tuned for improved resolution at higher polynomial order – $P = 3$, $\mu_0 = 0.005$, $s_\kappa = -0.65$ and $\kappa = 0.1$. For reference, the baseline setup used $P = 1$, $\mu_0 = 0.01$, $s_\kappa = -1$, and $\kappa = 0.1$. Adjusting these values is a crucial step of using the AV within compressible solver in the Nektar++ framework to ensure accurate flow representation in the entire domain. As discussed previously, the magnitude of artificial viscosity must be carefully balanced – sufficient to stabilise discontinuities, but not large enough to introduce excessive dissipation in the wake. Several configurations were tested, with $\mu_0 = 0.005$ ultimately chosen. This value was deemed optimal for the studied simulation. To account for the higher polynomial order, s_κ was also modified to limit AV application to localised regions. The results for $s_\kappa = -0.65$ confirm this behaviour – AV is concentrated near the shock (Figure 19a), producing a well-resolved discontinuity (Figure 19b). At the same time, its effect in the wake is moderate, hence no excessive smoothing is introduced. These settings were obtained largely through trial and error, suggesting that future work should explore more systematic approaches to link polynomial order with AV tuning.

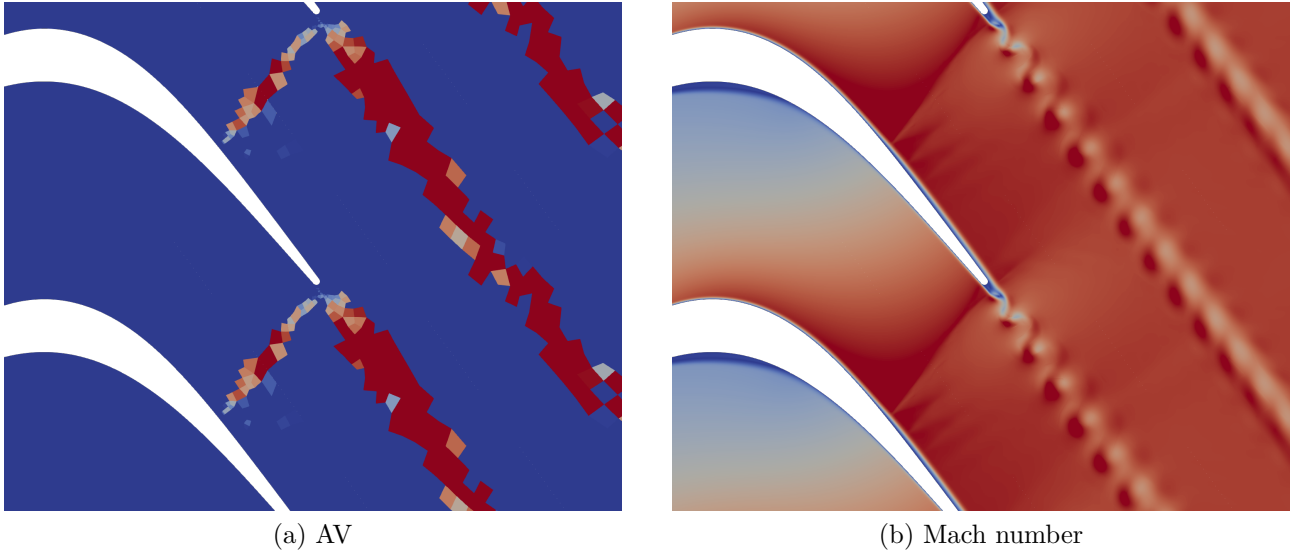


Figure 19: Results for the optimum AV settings.

5.3 Effect of Dimensionality

The following paragraph discusses comparison between dimensional and non-dimensional simulation runs. The central question addressed here is whether changing the simulation setup has a significant influence on the application of artificial viscosity.

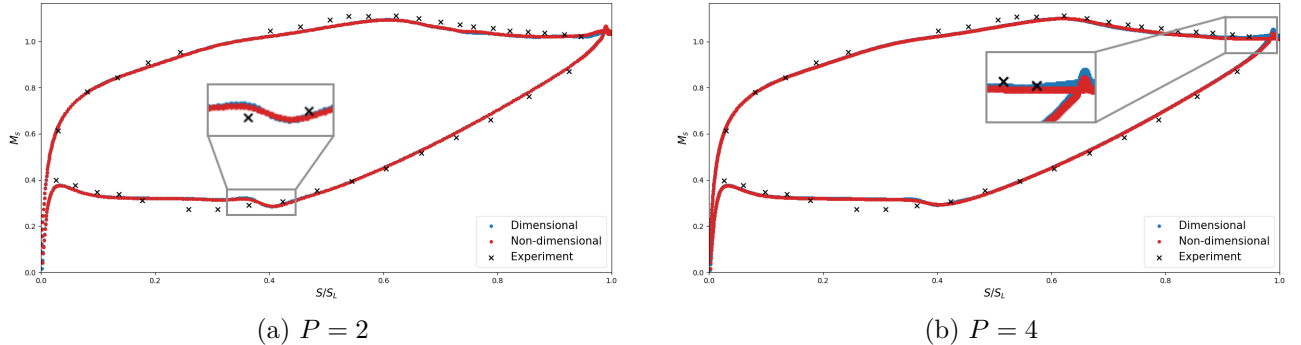


Figure 20: Time-averaged isentropic Mach number comparison between dimensional and non-dimensional setups for two polynomial orders ($M_{out} = 0.95$).

The analysis begins with a comparison of previously studied isentropic Mach number distribution plots. From Figure 20, it can be seen that the time-averaged blade loading is predicted consistently by both, with the two curves nearly overlapping across polynomial orders. This suggests that Nektar++ can reliably capture blade loading in practical applications. However, the graphs are not identical. The zoom-ins reveal discrepancies near the TE and on the pressure side, indicating that the two simulations differ in their behaviour along the blade. Although space- and time-averaged outlet Mach number does not change depending on the initial setup (Figure 21), it is important to perform a more detailed level of analysis to check that the flows are indeed identical.

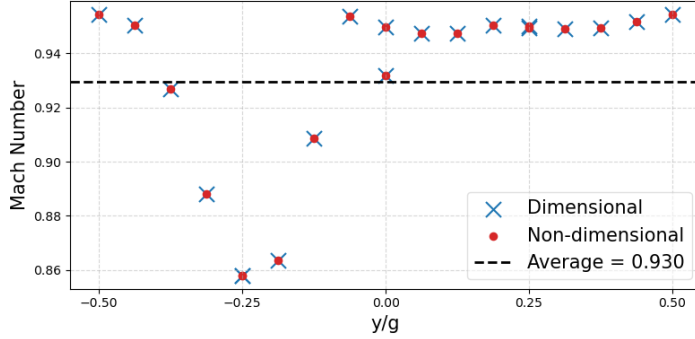


Figure 21: Time-averaged outlet Mach number. *Average* is the space average.

Figure 22 compares various quantities in the near-blade region. In both cases, the sensor (Figures 22a and 22b) highlights the same physical flow features, with elevated values (in red) across the shock region and within the wake; artificial viscosity is expected to be activated there for the purpose of numerical stabilisation. The main difference lies in the intensity and smoothness of the response. In the dimensional setup (Figure 22a), the sensor looks straighter than the non-dimensional case, which is more corrugated. In Figure 22b the neighbouring cells are energised unevenly and in a less orderly manner, which is particularly relevant when looking at the sensor result just below the TE. The discrepancies observed in the AV distribution mirror those of the sensor. In the dimensional case (Figure 22c), AV is activated for the shock in a slightly narrower region than in the non-dimensional setup (Figure 22d), consistent with the earlier sensor observations. Both simulations use identical threshold parameters, ensuring that artificial viscosity is triggered consistently. This might suggest that the source of the difference lies in the sensor behaviour rather than in the AV trigger. The impact is evident in the resolved flow – the shock appears sharper in the dimensional simulation, while in the non-dimensional case it is noticeably more diffused – see Figures 22e and 22f.

Several quantities were examined to identify the source of the discrepancy. Firstly, CFL numbers were compared across the simulation runs to confirm that timestep differences were not responsible. Apart from minor variations during the transient phase, which are acceptable, CFL values matched within 0.15%. Grid spacing was also checked to ensure that both cases maintained identical resolution relative to chord, ruling out mesh effects. Both simulations were initialised from RANS solutions, with the non-dimensional setup requiring a conversion step that introduced small errors in the conservative variables. These remained below 0.2% and although they inevitably influenced the initial state, the impact should not be large enough to explain the observed variation. Finally, since the sensor is calculated from density variations, any numerical artefact affecting density would influence the sensor response. Compressible disturbances were checked via the divergence field, but no clear link was identified.

Lastly, an additional investigation was carried out for the early CTUs, immediately after initialisation from the RANS solution to check whether the setup type produces different early-stage flow development. Figure 23 shows the AV applied at particular CTUs and the visualisations

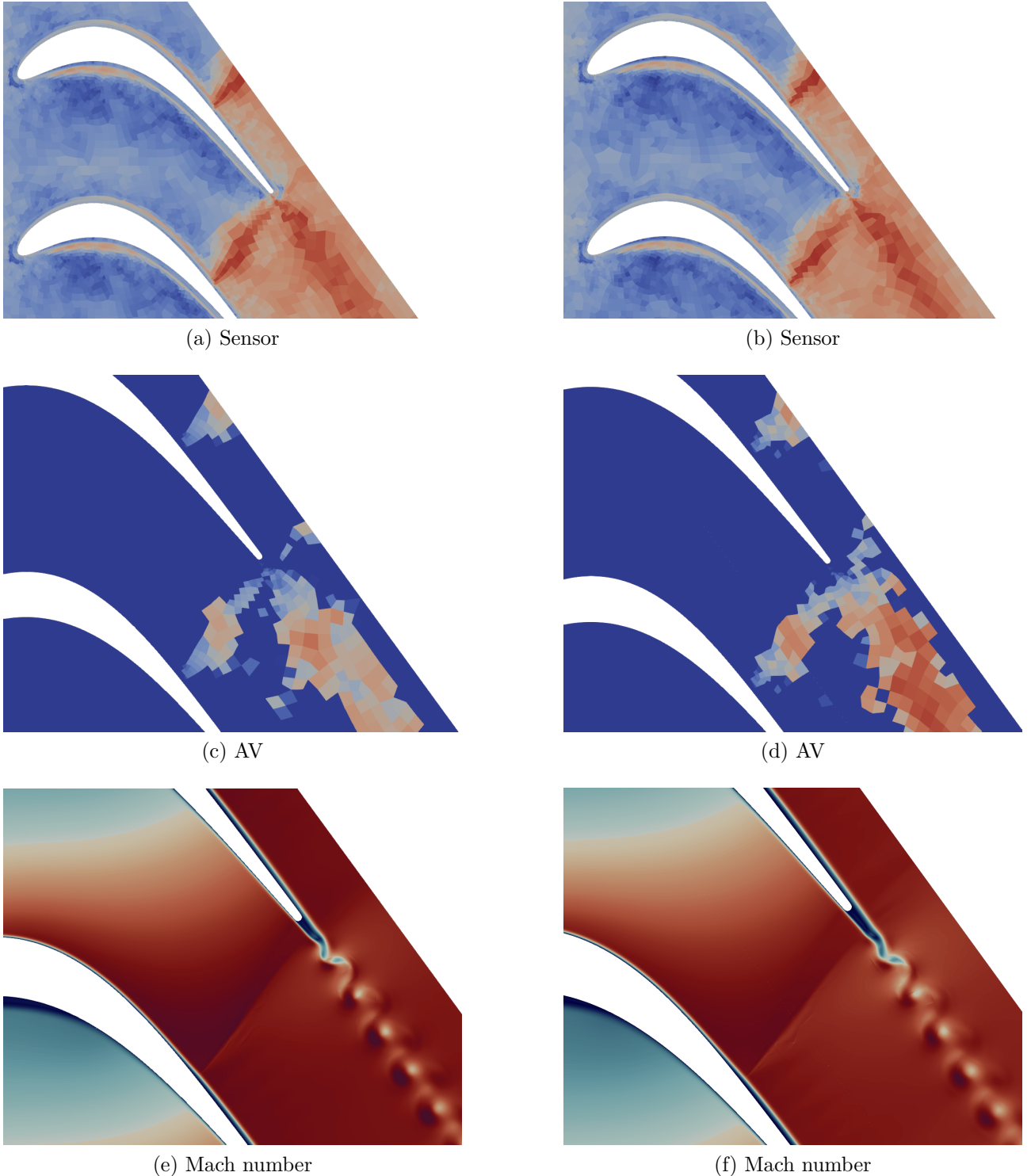


Figure 22: Instantaneous dimensional (left) and non-dimensional (right) quantities after 40 CTUs. Only two extruded domains were shown for visibility.

presented in Figure 26 (Appendix C) complement these by displaying corresponding Mach number flow fields. The comparative analysis reveals significantly different behaviour between the two setups. In the dimensional case (Figures 23a, 23c, 23e), noticeably more AV is added across the whole simulation, particularly near the domain inlet. Significant AV application is also required to stabilise the disordered transient flow after ≈ 4 CTUs, which is not the case for the non-dimensional run – see Figures 23c and 23d. Almost no AV is added in at the beginning

of the non-dimensional run (Figure 23b), suggesting a more gradual flow field evolution. Moreover, at $CTU = 4.5$ (Figure 23d), the AV distribution starts resembling the final state, implying quicker flow development. For largest CTU (Figures 23e and 23f), the AV visualisations look similar to those previously seen in Figure 22, where the dimensional simulation generally looks smoother. The larger initial AV application in the dimensional case is likely driven by the broader range of variable scales. In contrast, in the non-dimensional case, smaller differences may allow tiny numerical artefacts to persist, affecting AV behaviour. These differences in flow evolution likely introduce spurious effects that influence the subsequent AV application.

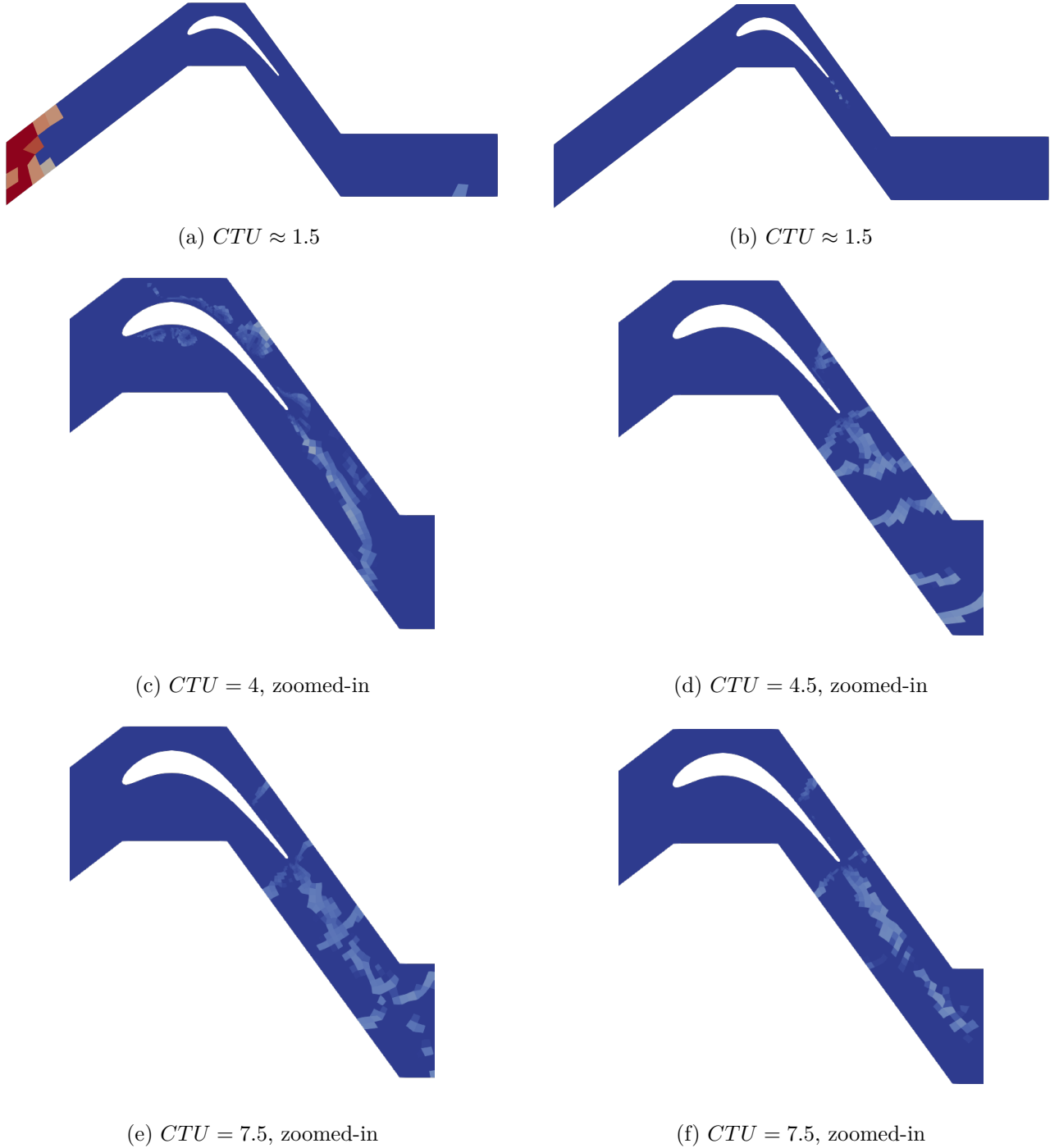


Figure 23: AV applied for dimensional (left) and non-dimensional (right) setups.

Comparing this to the Mach number visualisations (Figure 26), in the non-dimensional case, the flow indeed develops gradually and with little disorder, slowly flushing out the RANS field. In contrast, the dimensional run undergoes substantial changes: larger vortices form on the suction side and are subsequently convected out of the domain. This distinction is also evident in the modal energy evolution (Figure 24). While both simulations require more than ~ 7 CTUs to reach a statistically stationary state, the dimensional setup exhibits much larger variations in modal energy, consistent with earlier observations of its turbulent structures.

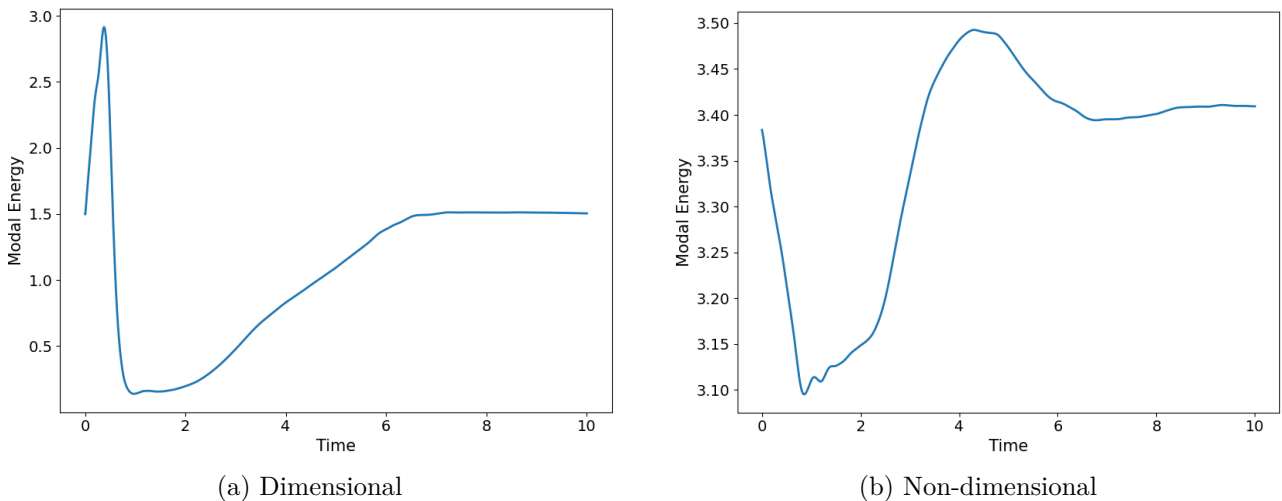


Figure 24: Modal energy evolution. *Time* on the x-axis denotes CTU.

In summary, artificial viscosity is applied inconsistently in the dimensional and non-dimensional runs. The sensor response varies between the runs, which the AV application follows. It indicates that the AV itself may not be the root cause, but rather sensitive to numerical artefacts in the domain. The non-dimensional case shows significantly different early flow evolution, which may introduce such artefacts. Overall, the non-dimensional setup yields less accurate results in this study, though further investigation is required to confirm the cause.

6 Conclusion and Future Work

6.1 Conclusion

The aim of this report was achieved through a detailed analysis of the simulation output. The flow field was examined and the resolution of key flow features was assessed qualitatively, demonstrating that Nektar++ successfully reproduced the overall flow behaviour and captured shocks (where present) to a satisfactory standard. The isentropic Mach number distribution confirmed that blade loading was well represented on the suction surface, particularly in the higher Mach cases where shocks were present. Nektar++ was shown to perform better than Star-CCM+, validating the suitability of spectral/hp element methods for turbomachinery applications. On the pressure surface, accuracy was limited by the absence of inflow turbulence, which also made the subsonic case ($M_{out} = 0.7$) unsatisfactory. Additional metrics, including

outlet Mach number and skin-friction coefficient, were also evaluated and found to be broadly consistent with trends reported in the literature. Overall Nektar++ provided a reliable representation of the high-speed low-pressure turbine flow.

Further analysis investigated the role of artificial viscosity, providing insight into its optimal settings and highlighting challenges at higher polynomial orders, where the reduced AV threshold increased dissipation, resulting in limited resolution despite the expectation of improved accuracy for higher P . While the discussion remained qualitative, it established a foundation for more systematic future studies. Finally, comparisons between dimensional and non-dimensional setups revealed differences in shock resolution and provided a preliminary explanation for the observed discrepancies. No evidence suggested errors in Nektar++ implementation; the differences may also be of numerical origin, which is why the topic requires further investigation.

6.2 Future Work

This study provides an initial analysis of the SPLEEN LPT cascade and the AV implementation in Nektar++, from which several directions for future work have been identified:

1. **Inflow turbulence:** Future work should include inflow turbulence to promote a more realistic BL transition process and assess whether Nektar++ captures BL behaviour correctly, to mitigate the influence of PS numerical bubble on the flow field.
2. **Quasi-3D simulations:** The present study was restricted to two-dimensional simulations. Since turbomachinery flows are inherently three-dimensional, extruding the computational domain and performing quasi-3D simulations would improve physical representation of flow features (e.g. vortices, wake losses).
3. **Artificial viscosity tuning:** The effect of polynomial order on AV behaviour should be studied in detail, with emphasis on developing a more informed methodology for selecting AV parameters. Moving beyond 'trial and error' tuning would increase both accuracy and reproducibility.
4. **Artificial viscosity investigation:** The current work provided foundation for exploring the AV implementation in Nektar++ but requires a more systematic and quantitative assessment to clarify the origin of discrepancies observed between dimensional and non-dimensional setups.

References

- [1] Gregory M. Laskowski, James Kopriva, Vittorio Michelassi, Sriram Shankaran, Umesh Paliath, Rathakrishnan Bhaskaran, Qiqi Wang, Chaitanya Talnikar, Zhi J. Wang, and Feilin Jia. Future Directions of High Fidelity CFD for Aerothermal Turbomachinery Analysis and Design. In *46th AIAA Fluid Dynamics Conference*, Washington, D.C., 2016. American Institute of Aeronautics and Astronautics. doi: 10.2514/6.2016-3322.
- [2] Mujeeb R. Malik and Dennis M. Bushnell. Role of Computational Fluid Dynamics and Wind Tunnels in Aeronautics R&D. Technical report, NASA Langley Research Center, 2012.
- [3] Margaret Wright. The Opportunities and Challenges of Exascale Computing. Technical report, U.S. Department of Energy, 2010.
- [4] Richard D. Sandberg, Vittorio Michelassi, Richard Pichler, Liwei Chen, and Roderick Johnstone. Compressible Direct Numerical Simulation of Low-Pressure Turbines—Part I: Methodology. *Journal of Turbomachinery*, 137(5), 2015. doi: 10.1115/1.4028731.
- [5] Zhi J. Wang. High-order methods for the Euler and Navier–Stokes equations on unstructured grids. *Progress in Aerospace Sciences*, 43(1-3):1–41, 2007. doi: 10.1016/j.paerosci.2007.05.001.
- [6] Joachim Kurzke. Fundamental Differences Between Conventional and Geared Turbofans. In *ASME Turbo Expo 2009: Power for Land, Sea and Air*, Orlando, Florida, USA, 2009. doi: 10.1115/GT2009-59745.
- [7] Maxime Borbouse, Nathan Deneffe, Mars Thys, Margaux Boxho, Michel Rasquin, Gustavo Lopes, and Sergio Lavagnoli. Direct Numerical Simulations of the SPLEEN cascade: a study of the impact of compressibility on transition and separation in a low-pressure turbine passage. In *16th European Turbomachinery Conference*, Hannover, Germany, 2025.
- [8] GE Aerospace. GE9X Engine, 2025. URL <https://www.geaerospace.com/commercial/aircraft-engines/ge9x>. [Accessed 11th August 2025].
- [9] Anirban Garai, Laslo Diosady, Scott Murman, and Nateri Madavan. DNS of Flow in a Low-Pressure Turbine Cascade Using a Discontinuous-Galerkin Spectral-Element Method. In *Volume 2B: Turbomachinery*, Montreal, Canada, 2015. American Society of Mechanical Engineers. doi: 10.1115/GT2015-42773.
- [10] Peter Vincent, Freddie Witherden, Brian Vermeire, Jin Seok Park, and Arvind Iyer. Towards Green Aviation with Python at Petascale. In *SC16: International Conference for High Performance Computing, Networking, Storage and Analysis*, pages 1–11, Salt Lake City, UT, 2016. IEEE. doi: 10.1109/SC.2016.1.
- [11] Guglielmo Vivarelli, João Anderson Isler, Francesco Montomoli, Chris Cantwell, Spencer J. Sherwin, Yuri Frey-Marioni, and Raul Vazquez-Diaz. Applications and Recent Developments of the Open-Source Computational Fluid Dynamics High-Fidelity Spectral/Hp Element Framework Nektar++ for Turbomachinery Configurations. In *Volume 12C: Turbomachinery — Design Methods and CFD Modeling for Turbomachinery; Ducts, Noise, and Component Interactions*, London, UK, 2024. American Society of Mechanical Engineers. doi: 10.1115/gt2024-125039.

- [12] Guglielmo Vivarelli, João Anderson Isler, Chris D. Cantwell, Francesco Montomoli, Spencer J. Sherwin, Yuri Frey-Marioni, Marcus Meyer, Iftekhar Naqavi, and Raul Vazquez-Diaz. A quasi-direct numerical simulation of a compressor blade with separation bubbles and inflow turbulence. *International Journal of Turbomachinery, Propulsion and Power*, 10(2), 2025. doi: 10.3390/ijtpp10020008.
- [13] Andrea Cassinelli, Hui Xu, Francesco Montomoli, Paolo Adami, Raul Vazquez Diaz, and Spencer J. Sherwin. On the Effect of Inflow Disturbances on the Flow Past a Linear LPT Vane Using Spectral/hp Element Methods. In *Volume 2C: Turbomachinery*, Phoenix, Arizona, USA, 2019. American Society of Mechanical Engineers. doi: 10.1115/gt2019-91622.
- [14] Andrea Cassinelli. *A spectral/hp element DNS study of flow past low-pressure turbine cascades and the effects of inflow conditions*. PhD thesis, Imperial College London, 2020.
- [15] Andrea Cassinelli, Andrés Mateo Gabín, Francesco Montomoli, Paolo Adami, Raul Vázquez Díaz, and Spencer J. Sherwin. Reynolds Sensitivity of the Wake Passing Effect on a LPT Cascade Using Spectral/hp Element Methods. *International Journal of Turbomachinery, Propulsion and Power*, 7(1):8, 2022. doi: 10.3390/ijtpp7010008. Publisher: MDPI AG.
- [16] Andrea Cassinelli, Francesco Montomoli, Paolo Adami, and Spencer J. Sherwin. High Fidelity Spectral/hp Element Methods for Turbomachinery. In *Volume 2C: Turbomachinery*, Oslo, Norway, 2018. American Society of Mechanical Engineers. doi: 10.1115/gt2018-75733.
- [17] João Isler, Guglielmo Vivarelli, Chris Cantwell, Francesco Montomoli, Spencer Sherwin, Yuri Frey, Marcus Meyer, and Raul Vazquez. Source Term-Based Synthetic Turbulence Generator Applied to Compressible DNS of the T106A Low-Pressure Turbine. *International Journal of Turbomachinery, Propulsion and Power*, 10(3):13, 2025. doi: 10.3390/ijtpp10030013.
- [18] Junjie Ye, Guglielmo Vivarelli, João Isler, David Moxey, Spencer J. Sherwin, and Chris D. Cantwell. High-fidelity sliding mesh method for moving geometries in turbomachinery applications. In *Proceedings of the 16th European Turbomachinery Conference (ETC16): Turbomachinery, Fluid Dynamics and Thermodynamics*, Hannover, Germany, 2025. European Turbomachinery Society (EUROTURBO). March 24–28, 2025.
- [19] Yuri Frey Marioni, Enrique De Toledo Ortiz, Andrea Cassinelli, Francesco Montomoli, Paolo Adami, and Raul Vazquez. A Machine Learning Approach to Improve Turbulence Modelling from DNS Data Using Neural Networks. *International Journal of Turbomachinery, Propulsion and Power*, 6(2):17, 2021. doi: 10.3390/ijtpp6020017.
- [20] Yuri Frey Marioni, Paolo Adami, Raul Vazquez Diaz, Andrea Cassinelli, Spencer Sherwin, and Francesco Montomoli. Development of Machine-Learnt Turbulence Closures for Wake Mixing Predictions in Low-Pressure Turbines. In *Proceedings of ASME Turbo Expo 2022*, Rotterdam, Netherlands, 2022. doi: <https://doi.org/10.1115/1.4066919>.
- [21] Nathan Deneffe. Numerical study of boundary layer stability and compressible flow phenomena in a high-speed low pressure turbine with elevated free-stream turbulence. Master's thesis, Université de Liège, 2024.
- [22] Maxime Borbouse and Nathan Deneffe. RANS study of the SPLEEN high-speed low-pressure turbine cascade. Technical report, Université de Liège, 2025.

- [23] Loris Simonassi, Gustavo Lopes, Samuel Gendebien, Antonino F. M. Torre, Marios Patinios, Sergio Lavagnoli, Nicolas Zeller, and Ludovic Pintat. An Experimental Test Case for Transonic Low-Pressure Turbines – Part I. In *Proceedings of ASME Turbo Expo 2022*, Rotterdam, Netherlands, 2022. ASME. doi: 10.1115/GT2022-81566.
- [24] Gustavo Lopes, Loris Simonassi, Antonino F. M. Torre, Marios Patinios, and Sergio Lavagnoli. An Experimental Test Case for Transonic Low-Pressure Turbines - Part 2. In *Proceedings of ASME Turbo Expo 2022*, Rotterdam, Netherlands, 2022. American Society of Mechanical Engineers. doi: 10.1115/GT2022-82626.
- [25] Per-Olof Persson and Jaime Peraire. Sub-Cell Shock Capturing for Discontinuous Galerkin Methods. In *44th AIAA Aerospace Sciences Meeting and Exhibit*, Reno, Nevada, 2006. American Institute of Aeronautics and Astronautics. doi: 10.2514/6.2006-112.
- [26] Garrett E. Barter and David L. Darmofal. Shock capturing with PDE-based artificial viscosity for DGFEM: Part I. Formulation. *Journal of Computational Physics*, 229(5): 1810–1827, 2010. doi: 10.1016/j.jcp.2009.11.010. Publisher: Elsevier BV.
- [27] David Moro, Ngoc Cuong Nguyen, and Jaime Peraire. Dilation-based shock capturing for high-order methods. *International Journal for Numerical Methods in Fluids*, 82(7): 398–416, 2016. doi: 10.1002/fld.4223.
- [28] Department of Aeronautics, Imperial College London, UK and Scientific Computing and Imaging Institute, University of Utah, USA. *Nektar++: Spectral/hp Element Framework User Guide*. Imperial College London and University of Utah, 2025. URL <https://www.nektar.info/src/user-guide-5.8.0.pdf>. [Accessed: 30th June 2025].
- [29] George Karniadakis and Spencer J. Sherwin. *Spectral/hp Element Methods for Computational Fluid Dynamics*. 2nd Edition, Oxford University Press, 2005.
- [30] Spencer J. Sherwin and Victor Ballester Ribo. Compressible Flow. AERO70024 Applications of CFD Blackboard Page, Imperial College London, 2025.
- [31] Zhen-Guo Yan, Yu Pan, Giacomo Castiglioni, Koen Hillewaert, Joaquim Peiró, David Moxey, and Spencer J. Sherwin. Nektar++: Design and implementation of an implicit, spectral/hp element, compressible flow solver using a Jacobian-free Newton Krylov approach. *Computers & Mathematics with Applications*, 2020. doi: 10.3929/ETHZ-B-000521761.
- [32] John D. Coull and Howard P. Hodson. Blade Loading and Its Application in the Mean-Line Design of Low Pressure Turbines. *Journal of Turbomachinery*, 135(2):021032, 2012. doi: 10.1115/1.4006588.
- [33] Sergio Lavagnoli, Gustavo Lopes, Loris Simonassi, and Antonino F. M. Torre. SPLEEN - High Speed Turbine Cascade – Test Case Database. doi: 10.5281/zenodo.13712768, 2024.
- [34] Christophe Geuzaine and Jean-François Remacle. Gmsh: A 3-D finite element mesh generator with built-in pre- and post-processing facilities. *International Journal for Numerical Methods in Engineering*, 79(11):1309–1331, 2009. doi: 10.1002/nme.2579.
- [35] Hermann Schlichting and Klaus Gersten. *Boundary-Layer Theory*. Springer, Berlin, Heidelberg, 2017. doi: 10.1007/978-3-662-52919-5.
- [36] Nicholas J. Georgiadis, Donald P. Rizzetta, and Christer Fureby. Large-eddy simulation: Current capabilities, recommended practices, and future research. *AIAA Journal*, 48(8): 1772–1784, 2010. doi: 10.2514/1.J050232.

A Solver Settings

Table 4: *SolverInfo* part of the Nektar++ session file.

Property	Value	Explanation
EQType	NavierStokesImplicitCFE	Equation that we want to solve (Compressible Navier-Stokes equations with Implicit discretization in time)
Projection	DisContinuous	Type of projection we want to use
AdvectionType	WeakDG	Advection operator - how we deal with advection (classical DG in weak form)
DiffusionType	InteriorPenalty	Diffusion Operator - how we deal with diffusion (Symmetric interior penalty method)
AdvectionAdvancement	Implicit	
DiffusionAdvancement	Implicit	
TimeIntegrationMethod	DIRKOrder2	Singly Diagonally Implicit Runge Kutta (Order 2) time integration
UpwindType	Roe	Type of numerical interface flux (Roe)
ProblemType	General	
ViscosityType	Variable	Variable viscosity through the Sutherland's law
ShockCaptureType	Physical	Add artificial viscosity to the physical viscosity
ShockSensorType	Modal	Use a modal sensor to identify where to add viscosity (see Sec. 9.4.1.2)
EquationOfState	IdealGas	

B Star-CCM+ Wake

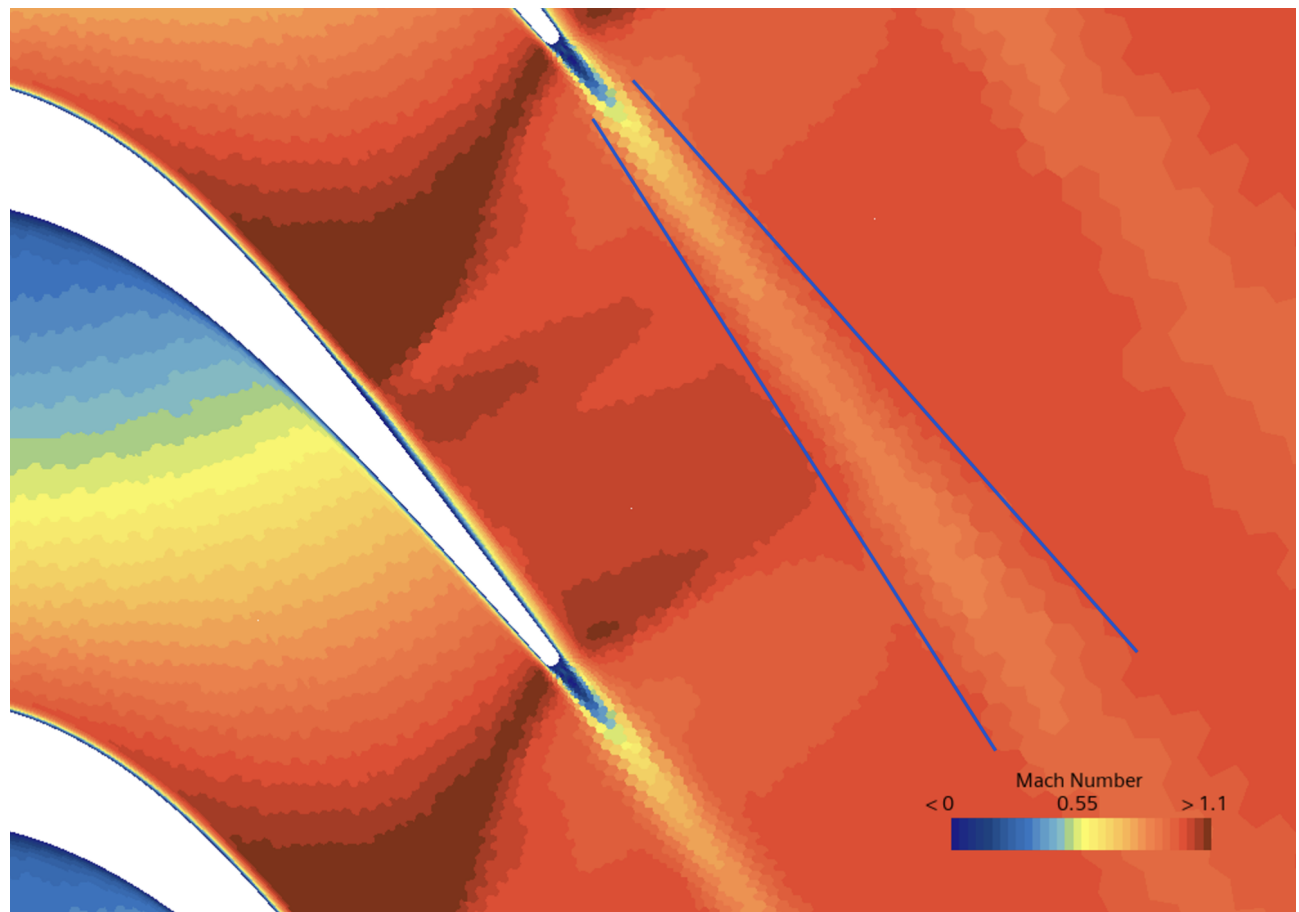


Figure 25: Wake Resolution from Star-CCM+ simulation ($M_{out} = 0.95$), showing the characteristic smooth, triangular wake with no unsteady oscillation.

C Artificial Viscosity Study Supplement

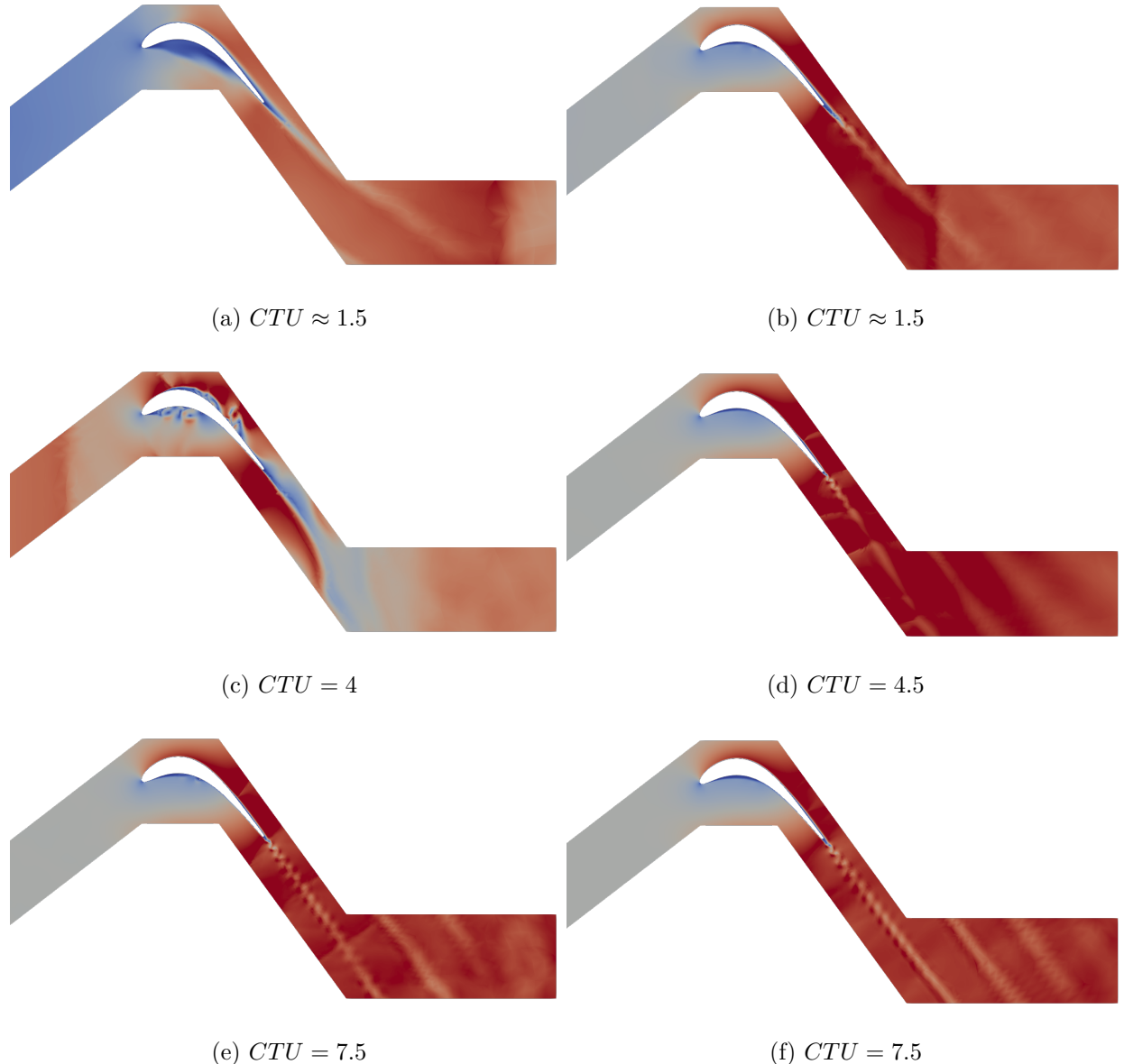


Figure 26: Mach number visualisations for dimensional (left) and non-dimensional (right) setups at different CTUs. One domain shown for visibility. The poor result quality is attributed to the fact that the simulations were run for $P = 1$.

D Star-CCM+ Tutorial

Turbomachinery Setup Guide for Star-CCM+

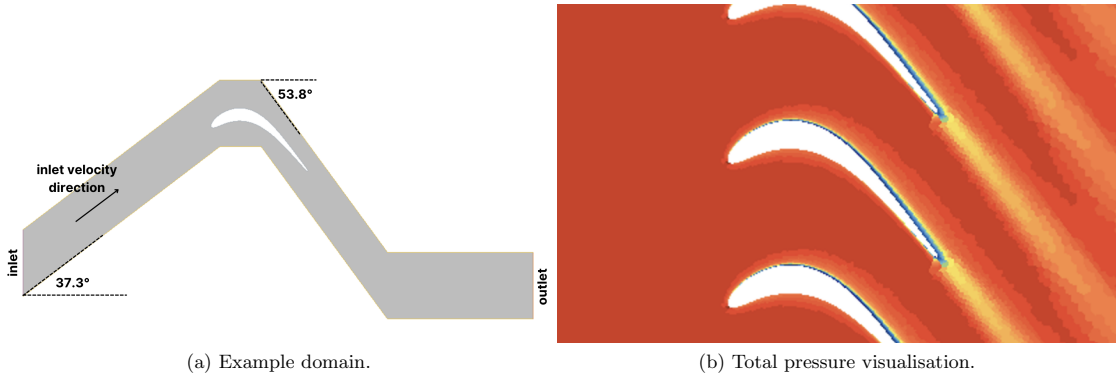
Mateusz Lisiewski

1 Introduction

This guide provides pathway to setting up two-dimensional turbomachinery simulations in Star-CCM+. Geometry and simulation data were taken from paper *Direct Numerical Simulations of the SPLEEN cascade: a study of the impact of compressibility on transition and separation in a low-pressure turbine passage* [1].

2 Example Problem Definition

The problem is given by domain in Figure 1a, which enables simulation of accurate flow around the blade. Note that the angle information was written on the domain to make it easier to set up as similar simulation for other cases. Simulating one blade is sufficient to obtain a good understanding of turbomachinery simulations, since periodic boundary conditions will be applied to bottom and top surfaces - see Figure 1b for post-processed total pressure field visualisation.



The following table summarises values used in the tutorial and are taken from [1].

Table 1: Boundary conditions for the example simulation.

Mach Number	$M_{s,out}$	0.7
Inlet Total Pressure	$p_{0,in}$	10779.39 Pa
Outlet Static Pressure	p_{out}	7771.16 Pa
Inlet Total Temperature	$T_{0,in}$	300 K
Inlet Flow Angle	α	37.3°
Outlet Flow Angle	α	53.8°

3 Boundary Conditions

3.1 Inlet

Inlet type is set as *Stagnation Inlet*, because this is well-suited for compressible internal flows [2]. It enables setting total pressure and total temperature upstream of the simulation domain. *Supersonic Static Pressure* option may rise some confusion, but it is actually quite simple. For subsonic inflow, then this value is ignored, and for supersonic flow it is calculated based on the isentropic relationship:

$$\frac{p}{p_t} = \left(1 + \frac{\gamma - 1}{2} M^2\right)^{-\frac{\gamma}{\gamma-1}} \quad (1)$$

where p is the supersonic static pressure, p_t is total/stagnation pressure, γ is the ratio of specific heats (for air this is 1.4) and M is Mach number [3]. Since in this case, the highest Mach number value is $M = 0.96$, it is expected that the flow will be not supersonic and that value is ignored. The rest of the entries are set as default, which includes *Turbulence Intensity* and *Turbulent Viscosity Ratio*.

Table 2: *Physics Values* for the inlet.

Property	Example Value
Flow Direction	Domain-dependant*
Supersonic Static Pressure	Irrelevant for Subsonic
Total Pressure	10779.39 Pa
Total Temperature	300K
Turbulence Intensity	Default
Turbulence Viscosity Ratio	Default

* Default direction is [1.0,0.0], which is along the x-axis. If the flow is inclined, then *Field Function* can be specified for the angle of incidence. Then the expression for *Flow Direction* is [$\cos(\text{angle_in})$, $\sin(\text{angle_in})$,0.0] assuming that `angle.in` is given in radians.

3.2 Outlet

Pressure Outlet option was chosen for the outflow condition, because it enables specification of outlet static pressure. There are multiple other properties that need to be carefully. Firstly, let us discuss the *Physics Conditions* that ought to be specified for this boundary type to be able to simulate turbomachinery. The paper that is used in this tutorial [1] explicitly specifies the outlet static pressure, which is why pressure at the outlet has to be kept constant. This is possible by setting *Backflow Pressure* is static, where "pressure is maintained at the specified pressure" [2]. The other values in *Backflow Specification* are set as default.

Table 3: *Physics Condition* choices for *Pressure Outlet* boundary type.

Property	Value
Backflow Specification	Direction
	Pressure
	Scalars
Pressure Outlet Option	None
Turbulence Method	Default

Pressure Outlet boundary type does not allow for explicit Mach number specification - instead *Static Temperature* is set, which can be recalculated using the isentropic relations:

$$\frac{T}{T_t} = \left(1 + \frac{\gamma - 1}{2} M^2\right)^{-1} \quad (2)$$

T_t is total/stagnation temperature and T is static temperature. Stagnation pressure can be assumed constant for this simulation, since adiabatic boundary conditions (BCs) are enforced on the boundary of the blade. For the example Mach number of $M = 0.7$, static temperature was calculated to be $T = 273.22K$. The rest of the values are taken from the paper [1].

Table 4: *Physics Values* for the outlet.

Property	Example Value
Pressure	7771.16 Pa
Static Temperature	273.22 K
Turbulence Intensity	Default
Turbulent Viscosity Ratio	Default

3.3 Periodic Boundaries

Periodic Boundary condition is set on the top and bottom boundaries of the domain by creating an *Interface*. Once the interface between the boundaries is established, as depicted in Figure 1, the *Topology* has to be set to *Periodic*.

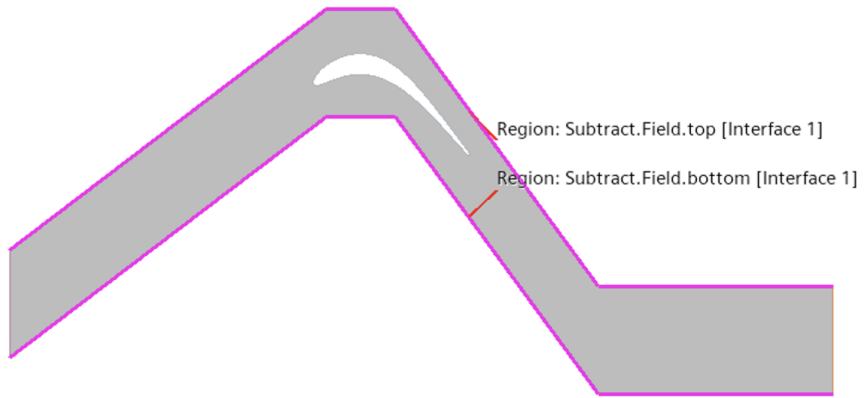


Figure 1: Interface between boundaries for the periodic BCs.

4 Initial Conditions

Inlet data is used to initialise *Pressure* and *Static Temperature*. Default values are used for other properties, for examples those defining turbulence. Should you need to change fluid type or its properties, you may do that by going to *Continua - Physics 1 - Models - Gas* and specifying correct values.

Table 5: Solver choices.

Property	Model
Material	Gas
Flow	Coupled Flow
Equation of State	Ideal Gas
Energy	Coupled Energy
Time	Steady
Viscous Regime	Turbulent
Turbulence	Reynolds-Averaged Navier-Stokes
Reynolds-Averaged Turbulence	Spalart-Allmaras Turbulence
Spalart-Allmaras Wall Treatment	All y+ Wall Treatment

5 Solver Choice

Turbomachinery flows are chaotic and characterised by unsteadiness, separation and potential local turbulence. The following *Physics Models* were chosen to simulate the flow accurately. The approach was followed from [2], namely *Tutorials - Compressible Flow - Subsonic Flow: NACA-Type Intake - Setting Up the Physics Models*.

6 Useful Information

If you're looking for definition of a property within Star-CCM+, highlight the property of interest and press *Shift+F1*. Star-CCM+ will launch the User Guide on the relevant page.

Relevant and potentially useful websites:

1. <https://volupe.com/simcenter-star-ccm/turbomachinery-workflow-in-simcenter-star-ccm/>
2. <https://docs.sw.siemens.com/documentation/external/PL20200805113346338/en-US/userManual/userguide/html/index.html#page/STARCCMP>
3. https://www.cfd-online.com/Wiki/Turbulence_intensity

References

- [1] Maxime Borbouse, Nathan Deneffe, Mars Thys, Margaux Boxho, Michel Rasquin, Gustavo Lopes, and Sergio Lavagnoli. Direct Numerical Simulations of the SPLEEN cascade: a study of the impact of compressibility on transition and separation in a low-pressure turbine passage. In *16th European Turbomachinery Conference (ETC16)*, Hannover, Germany, March 2025. Presented March 24-28, 2025. Available at <https://orbi.uliege.be/handle/2268/330117>.
- [2] Siemens Digital Industries Software. *Simcenter STAR-CCM+ User Guide (Online Documentation)*. Siemens Digital Industries Software, 2020. Version identified by internal ID PL20200805113346338.
- [3] Siemens Digital Industries Software. *How do I prescribe the supersonic static pressure*. Siemens Community, 2023.